Available online at BCREC website: https://bcrec.id

Bulletin of Chemical Reaction Engineering & Catalysis, 17 (3) 2022, 661-682

Research Article

Silicate Scaling Formation: Impact of pH in High-Temperature Reservoir and Its Characterization Study

Rozana Azrina binti Sazali[1,*], Kenneth Stuart Sorbie[2,3], Lorraine Scott Boak[2,3], Nurshazwani Shuhada binti Al Badri[1], Harumi Veny[1], Farah Hanim binti Ab Hamid[1], Mohd Zaki Zainal Abidin[1]

[1]School of Chemical Engineering, College of Engineering, Universiti Teknologi MARA, 40450, Selangor, Malaysia.
[2]Flow Assurance and Scale Team (FAST), Institute of GeoEnergy Engineering, Heriot-Watt University, EH14 4AS, Edinburgh, Scotland, United Kingdom.
[3]School of Energy, Geoscience, Infrastructure and Society (EGIS), Heriot-Watt University, EH14 4AS, Edinburgh, Scotland, United Kingdom.

Received: 23rd July 2022; Revised: 12th September 2022; Accepted: 12th September 2022
Available online: 21st September 2022; Published regularly: September 2022

Abstract

Silicate scaling tends to form and be aggravated during high pH Alkaline Surfactant Polymer (ASP) floods and this silicate scale deposition affects oil production. Hence, it is important to examine the conditions that lead to silicate scale forming. The severity of the silicate scaling reaction, the type and morphology of silica/silicate scale formed in an experimental ASP flood were studied for pH values 5, 8.5, and 11, whilst the temperature was kept constant at 90 °C. In addition, the impact of calcium ion was studied and spectroscopic analyses were used to identify the extent of scaling reaction, morphology type and the functional group present in the precipitates. This was performed using imagery of the generated precipitates. It was observed that the silica/silicate scale is most severe at the highest pH and Ca:Mg molar ratios examined. Magnesium hydroxide and calcium hydroxide were observed to precipitate along with the silica and Mg-silicate/Ca-silicate scale at pH 11. The presence of calcium ions altered the morphology of the precipitates formed from amorphous to microcrystalline/crystalline. In conclusion, pH affects the type, morphology, and severity of the silica/silicate scale produced in the studied scaling system. The comprehensive and conclusive data showing how pH affects the silicate scaling reaction reported here are vital in providing the foundation to further investigate the management and prevention of this silicate scaling.

Keywords: Silicate scale; Alkaline Surfactant Polymer Flooding (ASP); Amorphous silica scale; Metal silicates; Scale Morphology

How to Cite: R.A. Sazali, K.S. Sorbie, L.S. Boak, N.S. Al Badri, H. Veny, F.H. Ab Hamid, M.Z.Z. Abidin (2022). Silicate Scaling Formation: Impact of pH in High-Temperature Reservoir and Its Characterization Study. *Bulletin of Chemical Reaction Engineering & Catalysis*, 17(3), 661-682 (doi: 10.9767/bcrec.17.3.15290.661-682)

Permalink/DOI: https://doi.org/10.9767/bcrec.17.3.15290.661-682

1. Introduction

Enhanced Oil Recovery (EOR) is performed to regain to get back the oil production after the failure of natural drive and secondary recovery (water or gas) injection. One of the methods used during chemical injection is Alkaline Surfactant Polymer (ASP) flooding. The surfactants produced in situ during an ASP flood, formed by a reaction with the crude organic acids and alkali injection show the ultra-low interfacial tension (IFT). The presence of the polymer in the ASP flooding helps decrease the mobility of the

* Corresponding Author.
Email: rozana592@uitm.edu.my (R.A. Sazali);
Telp: +603-55436416, Fax: +603-55434300

water which contributes to the expansion of sweep efficiency and the ability to increase the viscosity of the fluid.

The primary aim of the surfactant is to reduce the IFT between fluid injection and residual oil in the reservoir and alter the wettability to water-wet which has been proven to enhance oil recovery. Whilst the alkali added is present to further reduce the IFT, alter the wettability and improve the emulsion via saponification [1–3]. Alkali reacts with natural acids (naphthenic acids) that are present in crude oils from the reservoir to develop in-situ surfactants (sodium naphthenate) through the saponification process causing a decrease in the interfacial tension bounded by oil and water to transfer additional quantities of oil to the well.

The improved retention of polymer in ASP readily improves the mobility ratio, which significantly enhances the sweep efficiency because of its capacity to increase the viscosity of the fluid [4–6]. More than 20 percent of the oil was recovered using an ASP flooding enhanced oil recovery technology when the Daqing oilfield became, the world's most outstanding ASP flooding case [7]. As stated, as the ASP flood is injected and progresses into the production well, the alkali reacts with the formation water and rock minerals triggers the increase of the scaling ions concentration, *i.e.* the calcium(II) ion (Ca^{2+}), the carbonate ion (CO_3^{2-}), and silicate anion (SiO_2^{3-}) within the production system. As the production fluid moves into or near the well, a significant change in pressure and temperature will be encountered. This results in the scaling ion equilibrium being altered causing the scale formation which has been explained by some as an increased concentration of reactive silica ions in the structure [8,9].

The production fluid and experiences significant changes in pressure and temperature as it passes adjacent or into the well, disrupting the scaling ion equilibrium resulting in the forming of scales. Changing pH can also alter silica solubility. A decrease in the pH value dissolves metal ions, such as Mg^{2+} and Ca^{2+}, in the formation and that increases the concentration of silica (by the dissolution of the formation rock due to the high initial pH of the ASP slug) causing supersaturation to happen. Hence, it is important to understand the factors that influence silicate scale formation. The silica/silicate scale is believed to be formed via four (4) stages which are silica dissociation, and silica polymerization before further either polymerising into pure long chain silica or bridging the metal ions into metal silicate scales. The silica/silicate scale may also co-precipitate with the calcium carbonate scale as further explained in detail below.

With respect to silica dissociation, the high pH of the ASP slug causes the dissolution reactions of quartz, SiO_2 (solid, crystalline) and amorphous silica, SiO_2 (solid, amorphous). This can be represented by Scheme 1:

$$SiO_{2\ (solid,\ amorphous)} + 2H_2O \leftrightarrow Si(OH)_{4\ (aqueous)}$$
$$SiO_{2\ (solid,\ crystalline)} + 2H_2O \leftrightarrow Si(OH)_{4\ (aqueous)}$$

(Scheme 1)

This monosilicic acid, $Si(OH)_4$ formed is later ionized to dissolved monomeric silica, $H_3SiO_4^-$ (also known as monosilicate ion or silicate ion), and can be expressed by Scheme 2:

$$H_4SiO_4^0 \leftrightarrow H_3SiO_4^- + H^+ \qquad \text{(Scheme 2)}$$

A study by Brown [10] reported that the solubility of amorphous silica under various pH conditions can be expressed by the following Equation (1):

$$S = C\left(1 + \left(\frac{10^{pH} \times K_1}{\gamma_{H_3SiO_4^-}}\right)\right) \qquad (1)$$

where, C is silica concentration in mg/L and can be calculated from $\log C = -731/T + 4.52$, T is an absolute temperature in Kelvin, where valid for 0 – 250 °C [11]; K_1 is the dissociation constant, which can be obtained with $\log K_1 = -2549/T - 15.36\times10^{-6}T^2$ (T in Kelvin); $\gamma_{H3SiO4-}$ is the activity coefficient of the ionized monosilicic acid that can be calculated from the Debye-Hückel equation and the ionic strength of the solution [12,13].

According to silica polymerization, ASP water at high pH travels through the formation to the near-wellbore (producer) region. As it flows, it comingles with the approximately neutral pH connate water generating a combined fluid mixture of lower pH. It is known that the solubility of monomeric silica decreases significantly at pH values below pH ~10.5. Under these lowered pH (and supersaturated) conditions, the dissolved monomeric silica begins to polymerize and colloidal silica nanoparticles start to form.

This simplest condensation reaction to form the neutral dimer is likely to proceed in Scheme 3. The silicate ion readily polymerizes by a dehydration reaction (by loss of H_2O molecule) that may build up to dimer $Si_2O(OH)_6$, trimer $Si_3O_2(OH)_8$, tetramer $Si_4O_3(OH)_{10}$, and so on.

With respect to silica scale formation, polymeric silicates can also form cyclic oligomer (instead of forming long-chain open structure – pyroxene) by linking the chain and eliminating the oxide where the most common cyclic polysilicates are the cyclic trimers, $(SiO_3)_3^{6-}$ and the cyclic hexamers, $(SiO_3)_6^{12-}$ (see Scheme 4).

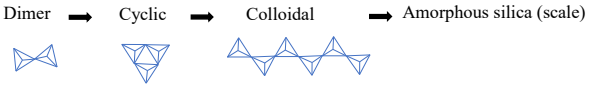

(Scheme 4)

The polymerized silicate may continue to grow and form a "pure" amorphous silica scale if there are no divalent cations present (Scheme 5).

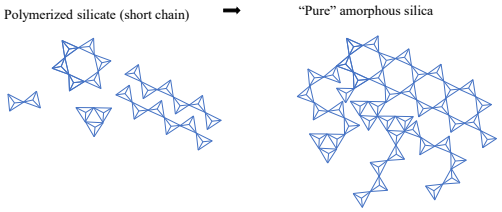

(Scheme 5)

Supersaturation occurs when the silica concentration is much higher than the solubility thus causing the amorphous silica scale to precipitate by both heterogeneous and homogenous pathways that are predominantly controlled by total silica concentration, silica monomer content, and temperature, while particle deposition is strongly affected by hydrodynamics [14]. Supersaturation of silica decreases as pH increases as the silica solubility increases (which reduce the tendency of the silica/silicate precipitation), however, in contrast, the rate of silica polymerization increases as pH increases generating the formation of amorphous silica scale [15]. As the ASP slug is injected, the pH of the injecting fluid that flows through the reservoir formation will experience changes in pH under different conditions.

In general, the solubility product, K_{sp} is the mathematical product of its dissolved ion concentrations raised to the power of their stoichiometric coefficients. For insoluble salts or slightly soluble salts, they are always in equilibrium. However, a real solution may not be in the state of equilibrium. This non-equilibrium state is described by the ion activity product, *IAP*.

The ratio between *IAP* and K_{sp} enters the definition of the saturation index, SI as shown in Equation (2):

$$SI = \log_{10} \frac{IAP}{K_{sp}} \tag{2}$$

The saturation index is a useful quantity to determine whether the water is saturated, undersaturated, or supersaturated concerning the given mineral;

$SI = 0$; $IAP = K_{sp}$ → saturated (in equilibrium)
$SI < 0$; $IAP < K_{sp}$ → undersaturated (no precipitation)
$SI > 0$; $IAP > K_{sp}$ → supersaturated (tendency to precipitate)

With respect to silicate scale (metal-silicate) formation, the presence of divalent cations such as Mg^{2+} and Ca^{2+} in the solution can affect the precipitation reaction where Meyers reported that silicate solubility decreases with pH when divalent cations were present [16]. The magnesium ion present in the connate/formation water may bridge the colloidal silicate particles to form an amorphous magnesium silicate scale. As the solution pH increases (especially at pH > 9), magnesium silicate scale is very likely to form because silica forms reactive silicate ions.

Hence, with the presence of Mg^{2+}, from the colloidal form explained earlier, silica scale forms as Mg^{2+}-poly-silicates (also true for Fe, Al, and Ca, but Mg^{2+} is the worst) (see Scheme 6).

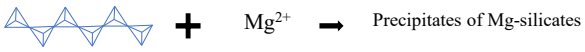

(Scheme 6)

According to co-precipitation of silicate scale with other minerals, the presence of calcium ions in the connate water will also promote the formation of a calcium carbonate scale which may additionally provide the nuclei for the development of silicate scales. A thorough review of previous work revealed that much research has been done on studying the mechanism involved in the formation of this silicate scale,

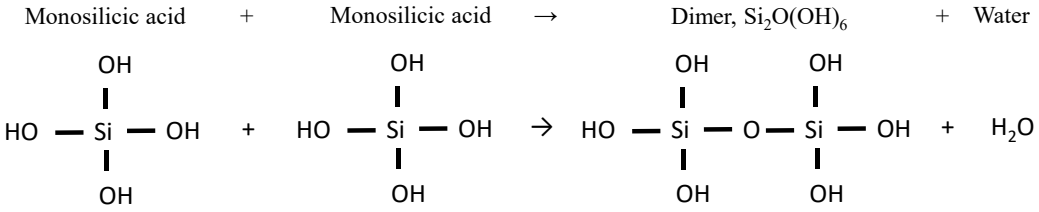

(Scheme 3)

however there is no detailed research done on the impact of pH variation on this type of scale in the ASP-flooded well environment. For instance, Jiecheng *et al.* [7] revealed that the scales formed in the ASP-flooded field are a combination of carbonate and silicate scale, but no information is available on the temperature/pH of the oilfield itself [7]. A study by Qing *et al.* reported a newly developed scale inhibitor to mitigate the silicate scale in an ASP-flooded Daqing oilfield, however, the SI formulation, as well as the reservoir condition, was not revealed [17]. Brown focused on the thermodynamics and the kinetic of pure amorphous silica formation, while Fleming and Crerar studied the silicic ionization and the solubility values; both worked in a geothermal well [10,18]. Kashpura and Potapov who also studied the possibility and methods of control for amorphous silica scaling from geothermal solution under conditions of Verkhne-Mutnovskaya geothermal electric power station, i.e. limited their investigation in the replicated environment of 250-300 °C and pH of 9.2 [19]. Whilst Lu *et al.* focused on developing a new inhibition efficiency testing for the scale inhibitor performance using the kinetic turbidity test (KTT) with the application of the Ultraviolet-Visible (UV-Vis) spectrophotometer, as an alternative to the dynamic tube blocking test due to the fact that the silica scale is very difficult to remove once they are formed [20]. Wang and Wei, on the other hand, contributed to the scale modelling, lab testing, and field trial observation to understand the silica/silicate scale formation in a steam-flooded well limited their study to wellbore condition of ~87.8 °C (and unknown pH condition) [21].

Therefore, this study aimed to investigate the changes in solubility, *i.e.* the effect of pH on the type, morphology, and severity of the silica/silicate scaling, to understand its formation mechanism in the ASP-flooded field. The presence of calcium ions was also investigated by varying the initial molar ratios of calcium with to magnesium ions, $(Ca:Mg)_o$. With current knowledge and these new findings examination of the inhibition (or at least reducing) of this silica/silicate scale in the ASP-flooded oilfield were investigated so that the silica/silicate management can be optimized.

2. Materials and Methods

2.1 Material

Silicon brine (SB) containing 1880 ppm of silicon ion (Si^{4+}) was prepared by dissolving 14.2 grams of sodium metasilicate pentahydrate ($Na_2SiO_3.5H_2O$) (Sigma Aldrich, ≥95.0% (T)) in 1 L of distilled water (DW) to represent the ASP slug. The magnesium brine (MB) solution was prepared by adding 15.05 grams of magnesium chloride hexahydrate salt ($MgCl_2.6H_2O$) (Merck, ACS reagent, 99.0-102.0%) in 1 L of DW to produce an initial concentration of 1800 ppm magnesium ions (Mg^{2+}).

Meanwhile, the various concentrations of calcium(II) ion, (Ca^{2+}) *i.e.* individual calcium brines (CB) were prepared by adding 4.1 grams, 8.2 grams, and 16.4 grams of calcium chloride hexahydrate salt ($CaCl_2.6H_2O$) (Sigma Aldrich, 98%) in 1 L of DW separately, to produce different initial concentrations of 750 ppm, 1500 ppm, and 3000 ppm Ca^{2+} respectively so that the effect of various initial of Ca:Mg molar ratios on silicate scale formation could be studied. Note that, Ca^{2+}, Mg^{2+}, and Si^{4+} ions are used exchangeably with Ca, Mg, and Si throughout this entire paper.

2.2 Methods

2.2.1 Brine mixing and conditions

All prepared brine solutions explained in section 2.1 were filtered using 0.45 μm filter paper. The brine solutions were mixed at appropriate volume as shown in Table 1 for a total of 7 experimental conditions. The brine solution in Experiments 1 and 2 contain Si ion only; while the mixed brine in Experiments 3 and 4 contain Si/Mg ions and Si/Ca ions respec-

Table 1. Final mixed brine concentration.

Experiment	Final Mix Concentration		
	Silicon (ppm)	Magnesium (ppm)	Calcium (ppm)
1 (Si only)	1880	0	0
2 (Si only)	940	0	0
3 (Si/Mg; Mg in excess)	940	900	0
4 (Si/Ca; Si in excess)	940	0	900
5 (Si/Mg/Ca; Ca:Mg=0.25)	940	450	187.5
6 (Si/Mg/Ca; Ca:Mg=0.5)	940	450	375
7 (Si/Mg/Ca; Ca:Mg=1)	940	450	750

tively; whereas the mixed brine in Experiments 5, 6, and 7 contain Si, Mg, and Ca ions with a variation in Ca:Mg molar ratios.

All mixed brines in the seven experiments were conducted at different initial pH conditions of pH 8.5, 5, and 11 which are denoted as Test Condition 1, 2, and 3 can be seen in Figure 1. The temperature of these mixed brines will be kept at a constant 90 °C to represent the reservoir condition. In the testing procedure, 50 mL of 1880 ppm silicon brine was added to 50 mL of 1800 ppm magnesium brine to produce a final mixed brine of 940 ppm Si and 900 ppm Mg (940Si:900Mg) in the test bottles, *i.e.* duplicate glass bottles 5 and 6, to get repeatable and reproducible results (Table 2). The initial pH of this mixed brine was checked, and the reading was recorded. The pH was adjusted to pH 8.5 (Test Condition 1) before being put into the oven at test temperature. They were allowed to react for 2 hours before the supernatant was sampled for further analysis to determine the relevant scaling ions, *i.e.* Si and Mg ions left in the supernatant using Atomic Absorption Spectroscopy (AAS) and the pH was checked. The glass bottles were then returned to the oven and allowed to react for another 20 h. The supernatant of the test solutions were sampled and the pH of the solution recorded. These final solutions were filtered through a 0.22 μm filter paper into a glass filtration unit and the precipitations formed were collected (if any).

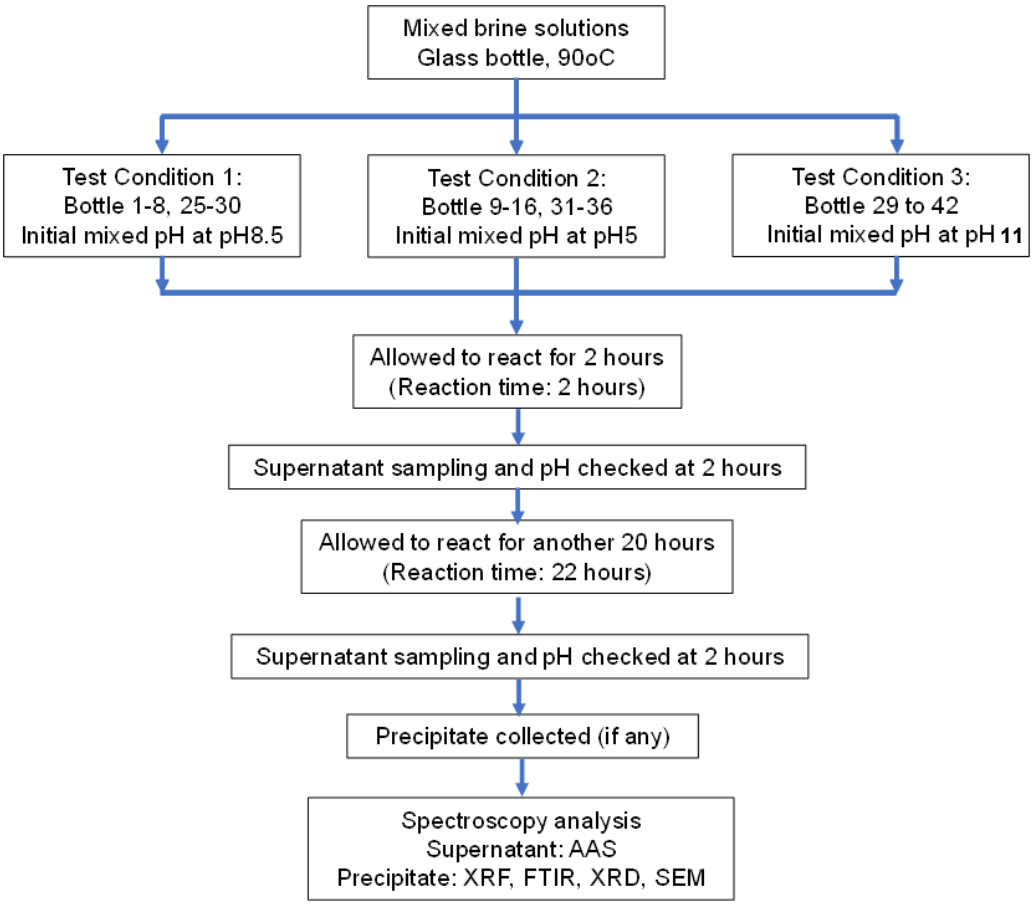

Figure 1. Experimental procedure for the effect of pH on silicate scaling test.

Table 2. List of the mixed solution in the glass bottle at test condition 1 (90 °C, pH 8.5).

Experiment	Glass Bottle	Initial Mixed Volume
1	1 & 2	100 mL 1880 ppm Si
2	3 & 4	50 mL 1880 ppm Si + 50 mL distilled water
3	5 & 6	50 mL 1880 ppm Si + 50 mL 1800 ppm Mg
4	7 & 8	50 mL 1880 ppm Si + 50 mL 1800 ppm Ca
5	25 & 26	50 mL 1880 ppm Si + 25 mL 1800 ppm Mg + 25 mL 750 ppm Ca
6	27 & 28	50 mL 1880 ppm Si + 25 mL 1800 ppm Mg + 25 mL 1500 ppm Ca
7	29 & 30	50 mL 1880 ppm Si + 25 mL 1800 ppm Mg + 25 mL 3000 ppm Ca

The precipitate collected was then dried in a desiccator for at least 24 h. The dried precipitates were crushed by a mortar turning them into a powder before being analyzed by various spectroscopic analysis techniques, such as Fourier transform infra red (FTIR), X-ray Diffraction (XRD), X-ray Fluorescence (XRF), and Scanning Electron Microscope/Energy Dispersive X-ray (SEM/EDAX). All steps were repeated for the other pH conditions of pH 5 (Test Condition 2) and pH 11 (Test condition 3) as shown in Tables 3 and 4, respectively. The methodology designed for this work was adapted from Sazali [22].

2.2.2 Atomic Absorption Spectroscopy (AAS)

Atomic Absorption Spectroscopy (AAS) model Hitachi Z-2000 located at the Instrumentation Laboratory II, School of Chemical Engineering, UiTM was used. Various appropriate concentrations of the standard solution for Ca and Mg were prepared. All these standard solutions were measured from the least to the highest concentration for the calibration curve setting. Between each analysis solution, a rinsing time of 30 seconds with the rinsing solution was used to clear carry over from the previous sample.

$$\textit{Metal cation reacted } [M]_{rx} = [M]_o - [M]_f \quad (3)$$

where, $[M]_o$ and $[M]_f$ are initial and final values of Mg^{2+} Ca^{2+}, and Si^{4+} concentration in the supernatant, respectively.

2.2.3 Fourier Transform Infrared (FTIR)

The FTIR spectra of the samples were obtained using Spectrum 100 spectrometer (PerkinElmer, USA) which is equipped with a mercury-cadmium-telluride (MCT) detector in the wavelength range from 650 to 4000 cm^{-1} and an universal attenuated total reflectance accessory (ATR) with a diamond prism. The FTIR spectra of all the samples were recorded on a Perkin Elmer Paragon 1000PC FTIR spectrometer using a diamond crystal. The spectra were measured in the wavenumber range 450-4400 cm^{-1}. The ability of the FTIR spectra range from 4000-400 cm^{-1} indicated all the possible functional groups present. The samples were crushed by the mortar to generate smaller particles. The smaller particles give a better spectra reading, while the larger particle tends to scatter the infrared beam and cause a slope of baseline and a poor spectra reading. This FTIR is also available at the Instrumentation Laboratory II, School of Chemical Engineering, UiTM.

2.2.4 X-Ray Diffraction (XRD)

A XRD RIGAKU /D/MAX 2200V/PC located in Drilling Laboratory, School of Chemical Engineering, UiTM was used to analyze the structure of materials from the scattering pattern produced by a beam of x-ray interacting with the experimental precipitate produced. It operated at experimental conditions 40 kV and 40 mA with a wavelength of Cu Kα 1.54 Å. This

Table 3. List of the mixed solution in the glass bottle at test condition 2 (90 °C, pH 5).

Experiment	Glass Bottle	Initial Mixed Volume
1	9 & 10	100 mL 1880 ppm Si
2	11 & 12	50 mL 1880 ppm Si + 50 mL distilled water
3	13 & 14	50 mL 1880 ppm Si + 50 mL 1800 ppm Mg
4	15 & 16	50 mL 1880 ppm Si + 50 mL 1800 ppm Ca
5	31 & 32	50 mL 1880 ppm Si + 25 mL 1800 ppm Mg + 25 mL 750 ppm Ca
6	33 & 34	50 mL 1880 ppm Si + 25 mL 1800 ppm Mg + 25 mL 1500 ppm Ca
7	35 & 36	50 mL 1880 ppm Si + 25 mL 1800 ppm Mg + 25 mL 3000 ppm Ca

Table 4. List of the mixed solution in the glass bottle at test condition 3 (90 °C, pH 11).

Experiment	Glass Bottle	Initial Mixed Volume
1	17 & 18	100 mL 1880 ppm Si
2	19 & 20	50 mL 1880 ppm Si + 50 mL distilled water
3	21 & 22	50 mL 1880 ppm Si + 50 mL 1800 ppm Mg
4	23 & 24	50 mL 1880 ppm Si + 50 mL 1800 ppm Ca
5	37 & 38	50 mL 1880 ppm Si + 25 mL 1800 ppm Mg + 25 mL 750 ppm Ca
6	39 & 40	50 mL 1880 ppm Si + 25 mL 1800 ppm Mg + 25 mL 1500 ppm Ca
7	41 & 42	50 mL 1880 ppm Si + 25 mL 1800 ppm Mg + 25 mL 3000 ppm Ca

wass then matched to an existing database to determine the chemical components within the material with a continuous scanning range of $2\theta = 10 – 90°$ for 3 min per sample.

2.2.5 X-Ray Fluorescence (XRF)

The percentage composition of each chemical component within a particular chemical in the precipitates was determined using a Malvern PANanalytical Zetium 4 kW. This was available in the Drilling Laboratory, School of Chemical Engineering, UiTM. The samples were mounted in a dedicated holder that has been exclusively designed for samples of irregular shapes and different sizes, where a small clamping device is available in the holder for accurate positioning of small samples and to avoid damage to samples.

2.2.6 Scanning Electron Microscope/ Energy Dispersive X-Ray Spectroscopy (EEM/ EDAX)

A Hitachi SU3500 15 kV SEM/EDAX located at the Material Science laboratory, School of Mechanical Engineering, UiTM was used to record the surface morphology of all precipitates. After sprinkling the powdery precipitates (specimen) on the double-sided conductive adhesive tape, excess powder was blown off using a blower. The specimen stub was set on the specimen holder and a vacuum level for observing a specimen (VP-SEM or SEM) in the [Vacuum mode] on the [Optics] tab on the operation panel was selected.

3. Results and Discussion

3.1 Observation

The physical observation of the effect of pH on silicate scaling formation was monitored and photographed. Three different pH conditions of pH 5, pH 8.5, and pH 11 were studied while the temperature was kept constant at 90 °C to represent reservoir conditions. The observations of each condition were recorded and explained in detail below.

Part A: Si-containing brine alone (to replicate ASP slug)

For the Si-containing brine only solutions shown in Figure 2, a clear solution remained for 22 h once the fluids were adjusted to pH 8.5 and pH 11. The acidic environment of pH 5 caused a cloudiness to be observed and during 22 h this became more of a jelly like precipitate.

Part B: Si/Mg/Ca - containing brine (to replicate the mixed brine of ASP slug with the presence of Mg ion and Ca ion in formation water)

Generally, as for the other Si/Mg/Ca scaling solution, a cloudy solution appeared as soon as the solutions were mixed (and the pH of the solution was adjusted) as can be seen in Figure 3.

With respect to Si/Mg mixed brine, for a final mixed Si/Mg brine of 940Si:900Mg, a cloudy solution instantly appeared at all pH values tested. Figure 3(a) (bottom) shows that the 940Si:900Mg at an initial pH 11 produced the highest amount of precipitates followed by Test Condition 1 (pH 8.5) and Test Condition 2 (pH 5). This shows that the mixed brine at pH 11 experienced the most severe scaling reaction, this may be due to the co-formation of magnesium hydroxide in addition to the Mg-silicate scale *e.g.* ($MgSiO_3$); a magnesium salt of silicic acid that containing magnesium oxide (MgO) and silicon oxide SiO_2 with an unspecified amount of water was formed.

With respect to Si/Ca mixed brine, experiments were conducted to study the effect of pH on the initial Si/Ca mixed brines of

Figure 2. Physical observation after 22 h of reaction time for Si-only containing brine with 1880 ppm Si (left) and 940 ppm Si (right).

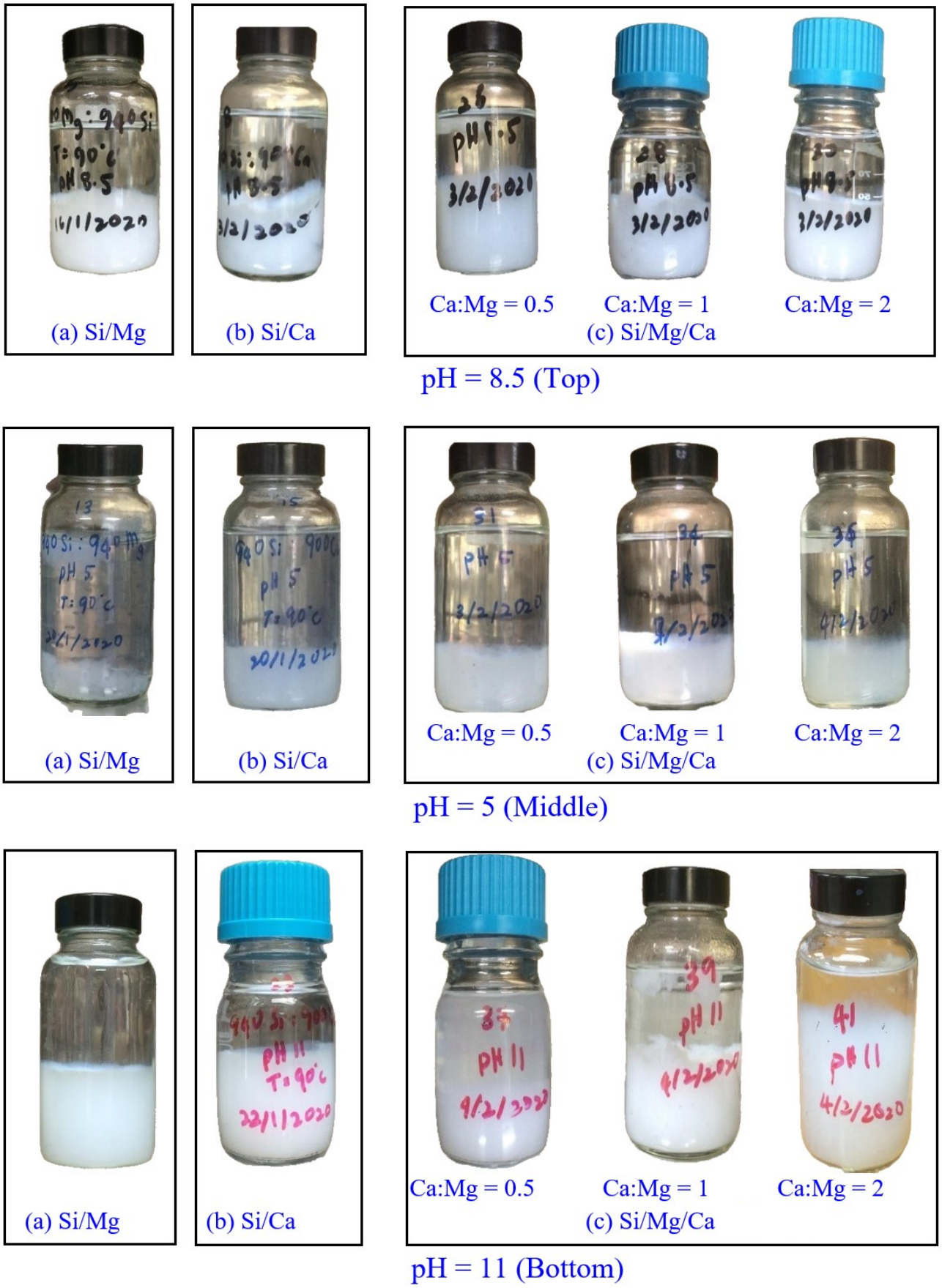

Figure 3. Physical observation of Si/Mg/Ca containing brine with various concentrations at pH 8.5 (top), pH 5 (middle), pH 11 (bottom) at 0 hours, *i.e.*, immediately after being mixed and pH adjusted.

940Si:900Ca, *i.e.* initial pH of 8.5, 5, and 11, respectively. All of these mixed brines turned into cloudy solutions immediately after pH-adjusted and became more prominent at 22 h, for all pH conditions. This occurrence is probably because of the effects of the initial pH play in the silicate scaling reaction. At these high pH conditions, the silicic acid dissociates into silicate anion (SiO_3^{2-}) which tends to react with a high concentration of calcium ion (Ca^{2+}) present.

In addition to that, the presence of the calcium ion in the solution may decrease the solubility of the silica ion that creating a supersaturation condition that leads to the polymerization of the silica ion and the bridging of this polymerized silica with the calcium ion. Based on these arguments, we can directly correlate the haziness/cloudiness/precipitate that appeared at the bottom of the test samples with the amounts of silicate scaling formed as can be seen in Figure 3(b). These must be confirmed through AAS analysis, though. At acidic conditions, it can be seen that the precipitate was much lesser compared to the alkaline condition. This may be due to the silicic acid did not dissociate much to form the silicate anion.

Focusing on Si/Mg/Ca mixed brine, the same observations and findings can be seen from Figure 3(c) which studies the Si/Mg/Ca mixed brines with different Ca:Mg molar ratio concentrations that explain the cloudy formation immediately formed after being pH adjusted. However, we cannot confirm the extent of the reactions for all Ca:Mg molar ratios tested by only observing the reactors, so that the supernatants were sampled and analysed in AAS and are discussed in the following section.

3.2 AAS Results and Data Analysis: Severity of Silicate Scaling and Extent of Reaction

The supernatants of the mixed brine were quenched into 1% EDTA/NaOH quenching solution before being analysed using AAS to determine the extent of reaction of metals ion presented in the solution, *i.e.* Mg^{2+} and Ca^{2+}. The extent of reaction was evaluated using the amount of metal cations which has reacted according to Equation (1).

According to Sazali *et al.* what is measured in these experiments (by AAS) is the concentration of [Mg] and [Ca] *remaining* in the solution after any silica/silicate precipitation has occurred [22,23]. However, it is convenient here to plot the amount of Mg or Ca which has *reacted*, i.e. the amount missing from the solution, which we refer to as the "*ion reacted*" (since it is in the precipitate).

The AAS results for the three pH conditions studied were further analysed and graphed in Figure 4. It can be seen that for pH 8.5, the percentage amount of magnesium ion reacted was increased from 68.8% to 70.5% at 2 h and 22 h respectively. The results suggest that at pH 8.5, the reaction between magnesium and silica tends to form a metal silicate which was magnesium silicate in addition to the amorphous silica scale. At pH 5, it was observed that 66.3% and 65.7% were reacted at 2 h and 22 h respectively. It is postulated that at a pH lower than pH 8.5, the magnesium ion did not react with silica thus "NO" metal silicate formed as no ionization and no monomeric that could polymerize a unionized silicic acid. However, in this experiment, the temperature was kept very high at 90 °C, which that sufficiently high to initiate and aggravate the Mg-silicate scale formation where the magnesium silicate scale exhibited inverse solubility [24–26]. It was observed that 95.8% of magnesium was reacted at 22 h, and this had increased to 97.6% at 22 h when the mixed Si/Mg was left reacted at pH 11. This may be due to that at a high pH value of 11, the magnesium ions were also reacted to with hydroxyl ion (OH^-) forming the magnesium hydroxide $Mg(OH)_2$, in addition to the formation of the Mg-silicate scale.

AAS analysis on the amount of Ca ion reacted at different pH conditions corresponding by the time is taken shown in Figure 5. Generally, the amount of Ca ion reacted in Si/Ca mixed brine was less than the amount of Mg ion reacted in Si/Mg mixed brine at all pH studied. At pH 8.5, it was found that only 30.7% and 26.3% of Ca ions reacted at 2 h and 22 h respectively; whereas these amounts were 24.4% and 30.7% at pH 5. This may suggest that the Mg^{2+} has a greater impact than Ca^{2+}, that the

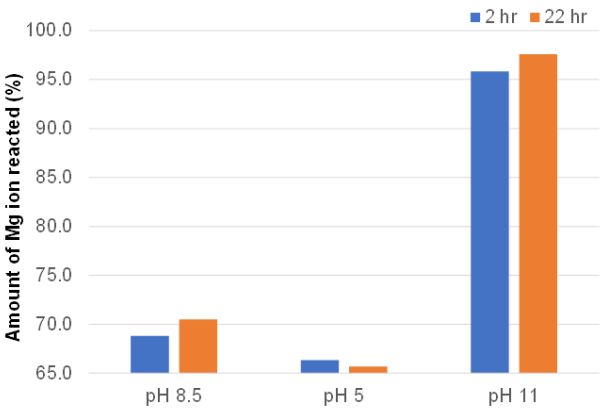

Figure 4. Percentage amount of Mg ions reacted under different temperature conditions for 940 ppm Si : 900 ppm Mg scaling brine.

silica backbone has a higher tendency to bridge the Mg^{2+} than Ca^{2+} which agrees with Hauksson *et al.* [27] that reported commonly encountered cations affect solubility in the order of Mg > Ca > Sr > Li > Na > K. However, AAS results show these values were substantially high at pH 11 with 92.8 and 91.9% at 2 h and 22 h, respectively. The potential of calcium silicate formed was higher where the high temperature of 90 °C sufficiently leads to scale acceleration. The Si:Mg molar ratios and Si:Ca molar ratios in the precipitates formed in both Si/Mg and Si/Ca scaling solutions were further analysed in Figure 6. The amounts of ions reacted as calculated by Equation 1 were eventually converted into Si:Mg and Si:Ca molar ratios in the solid silicate scale and these can be compared to ESEM/EDAX analysis.

The AAS results established that the resultant Si:Mg molar ratios in the precipitates is approximately 1 at all pH, when the Mg was in excess initially as compared to Si ion, i.e. $(Si:Mg)_o \approx 0.9$. This means, approximately 1 mol of magnesium is bridged to 1 mol of silicon ion. This complemented the Si:Mg molar ratio in precipitates that measured via inductively coupled plasma optical emission spectrometry (ICP-OES) reported by Sazali *et al.* [23]. They reported that the Si:Mg molar ratio in the precipitates were ~1.3 and ~1 at pH 8.5 and pH 10.1, respectively which is comparable with results reported om Figure 6 (Si:Mg molar ratio in the precipitates were ~1.2 and ~0.9 at pH 8.5 and pH 11, respectively). It is worth noting that the Si/Mg mixed brine was left reacted at room temperature (as opposed to 90 °C in this work); this may explain a little bit of deviation of the values at the same pH. From these analyses, it is clear that the pH values of the mixed brine are the most affecting factor as compared to the effect of temperature.

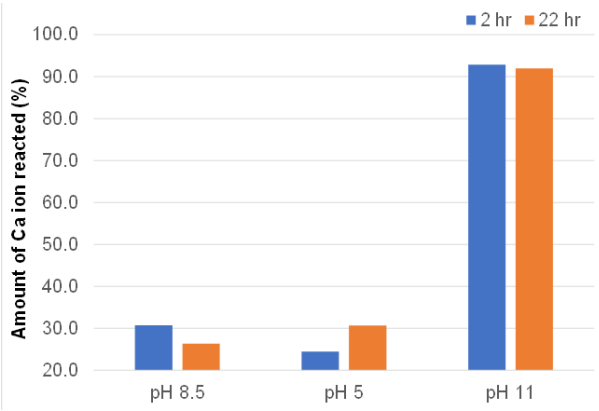

Figure 5. Percentage amount of Ca ions reacted under different pH conditions for 940 ppm Si: 900ppm Ca scaling brine.

This however was different in the Si-excess condition in the *i.e.* $(Si:Ca)_o \approx 1.5$ in the Si/Ca scaling environment solution; where the resultant Si:Ca molar ratios of more than 4 in the precipitates formed at pH 8.5 and pH 5. It was observed Si:Ca was found to be 5.3 and 4.7; at pH 8.5 and pH 5.0, respectively. This may be due to the polymerization of silica that occurred before the calcium ion reacted with the silica backbone. This is also in agreement with Hauksson *et al.* [27] that reported that Mg ion has a higher tendency to bridge the Si backbone as compared to Ca ion. In contrast, the Si:Ca was found to have remained approximately 1.5 at pH 11. This may suggest that the solubility of Ca ion is reduced significantly at high pH that aggravating the formation of calcium silicate scale that lead to more Ca ion bridged the Si backbone. Also, it is postulated more Ca^{2+} was reacted to form $Ca(OH)_2$ in addition to Ca-silicate and SiO_2 in this high pH of 11.

Figure 7 shows that the Ca:Mg molar ratios in the precipitates formed in various initial Ca:Mg molar ratios at all pH values tested. Generally, the Ca:Mg molar ratios increase with an increasing amount of Ca initially present at all pH's tested. At pH 8.5, a lower molar ratio of Ca:Mg was observed in the precipitates as compared to their initial molar ratios. This indicates that silicates favour Mg ions when both Ca and Mg ions are present at this pH condition. In contrast, higher molar ratios of Ca:Mg in precipitate were observed (as compared to their initial Ca:Mg molar ratios) at the lower pH 5 and higher pH 11 conditions. However, it is well known that the solubility of calcium silicate is much higher than that of

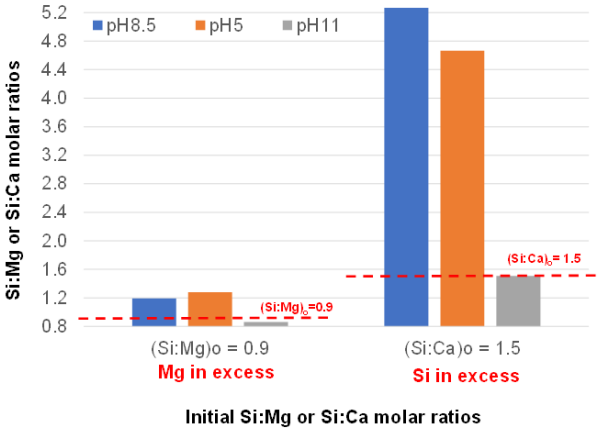

Figure 6. Si:Mg and Si:Ca molar ratios in the precipitates formed in Experiment 3 (940Si:900Mg) and Experiment 4 (940Si:900Ca) at various pH conditions.

magnesium silicate, hence could explain the initial removal of silica as magnesium silicate.

Similar to aluminum silicate SiO_4-Al, calcium carbonate $CaCO_3$, and calcium sulfate $CaSO_4$, Mg-silicate and Ca-silicate also show inverse solubility [28]. Therefore, as expected higher Mg-Ca-silicates were observed for this test temperature of 90 °C. This inverse or retrograde solubility may best be explained by the Le-Chatelier principle which states that dynamic equilibrium is disturbed by changing the conditions, and hence the position of equilibrium moves to counteract the change. Both Mg-silicate and Ca-silicate evolve heat when they are dissolved. For instance, the solution of solute (*i.e.* Mg^{2+} and Ca^{2+}) in water generates heat, hence, the position of the equilibrium will shifts left in the direction of the endothermic process to counter the disturbed equilibrium. As a consequence of this, the dissolution process will be slowed down. There will be more undissolved solutes, *i.e.* Mg-silicate and Ca-silicate in water.

The magnesium silicate system is highly pH -dependent. Essentially no Mg-silicate is expected to form at any pH less than 7 whereas magnesium silicate is very likely to form at higher pH due to the reactive silicate ions formed. However, as mentioned earlier, if the temperature is sufficiently high, precipitates may be seen at a much lower pH. It was observed in Figure 8 that around 30 to 34% of Mg ions reacted at pH 5 (and 90 °C) where the amount reacted seemed to reduce as the initial concentration of Ca ions present was increased. This was also true for the higher pH 8.5. At pH 11, it was observed that all Mg and Ca reacted. This may be due to some of the ions having reacted with the hydroxyl ion to form $Mg(OH)_2$ and $Ca(OH)_2$ in addition to the formation of the Mg-Ca-silicates scale.

Figure 9 shows that the amount of Ca ion reacted increased with a pH increase. The AAS results suggested that Ca^{2+} and Mg^{2+} were acting as the catalyst for the silica polymerization reaction. As mentioned earlier, Mg^{2+} has a greater impact than Ca^{2+}, which indicated that Mg^{2+} is precipitated out first before the Si backbone starts to bridge Ca^{2+}. The formation of Mg-SiO_4 is a two-step process. Generally, $Mg(OH)_2$ will form first and become inversely soluble with temperature. This is followed by the deposition of silicic acid $Si(OH)_4$ on a solid surface which condenses with any pre-existing solids surface that bears hydroxyl OH groups or any MOH, where

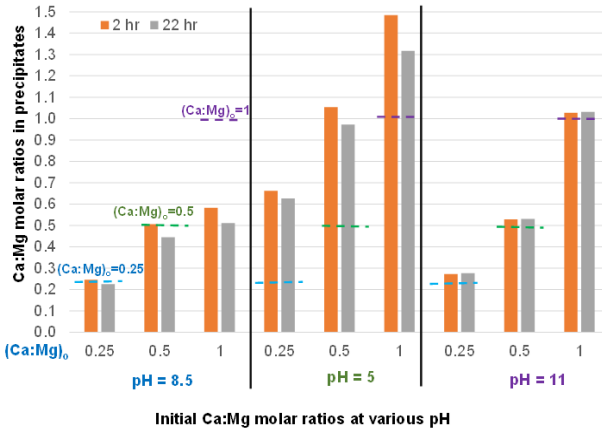

Figure 7. Ca:Mg molar ratios in the precipitates formed in Experiment 5 (940Si:450Mg:187.5Ca), Experiment 6 (940Si:450Mg:375Ca) and Experiment 7 (940Si:450Mg:750Ca) at various pH conditions.

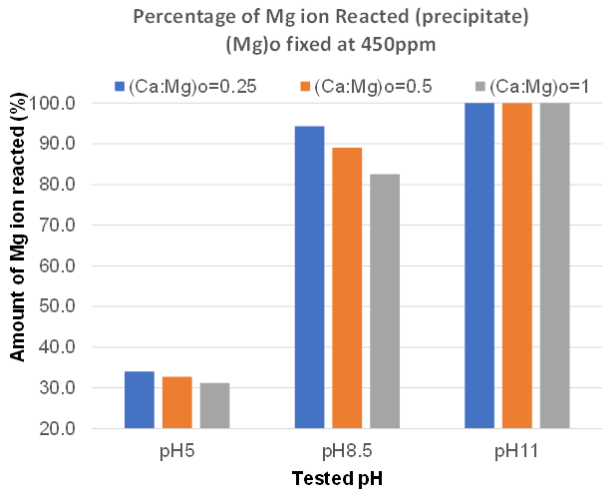

Figure 8. The percentage amount of Mg ion reacted in the presence of various Ca ion concentrations at various pH conditions.

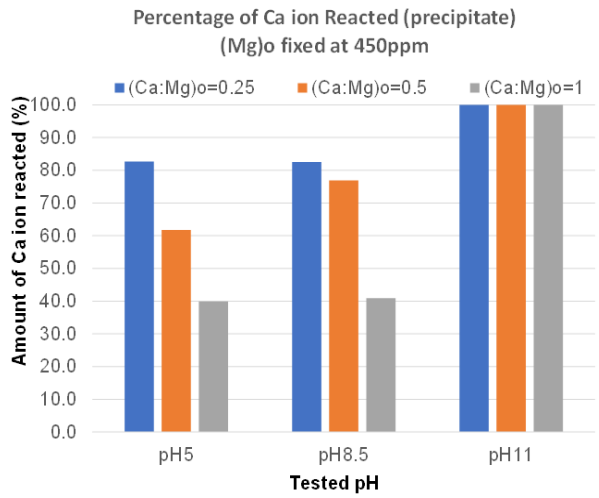

Figure 9. The percentage amount of Ca ion reacted when the initial Ca:Mg ion concentration varied at pH value tested.

M is a metal that will form silicate at the pH involved. The high percentage of Mg^{2+} and Ca^{2+} reacted indicates that the co-precipitation of $Mg(OH)_2$ and colloidal silica occurs.

3.3 XRF Results: Elemental Composition of the Metal-Silicate Scales

XRF analysis showed the percentage of magnesium, calcium, and silica concentration in the precipitates. The XRF results also indicate the composition of the precipitate where the 100% for every mixed solution concentration at all pH conditions is broken into its constituents. Figure 10(a) shows that the percentage of Mg in the precipitates increases as pH increased, which agrees with the AAS results shown in Figure 4. The low concentration detected at pH 5 suggested that the Mg ions were involved in any reactions under these acidic conditions. The XRF data in Figure 10(b) shows the highest percentage of calcium concentration was observed at pH 11. This suggested that more Ca ions have to bridge the silica backbone to form calcium silicate. The percentage of calcium concentration increased when pH increased from 5 to 8.5 and 11 due to lower calcium solubility at higher pH. This Si/Ca pattern similar to the Si/Mg mixed brine also agrees with the AAS result presented in Figure 5. The Figure 11 shows the percentage concentration of calcium in the precipitates increases as the concentration of Ca in the Si/Mg/Ca mixed brine increased from Ca:Mg is 0.25 to 0.5 and 1 at all pH values. At pH 5 (Figure 11(a)), the presence of Mg and Ca ion in the mixed brines has aggravated the polymerization of amor-

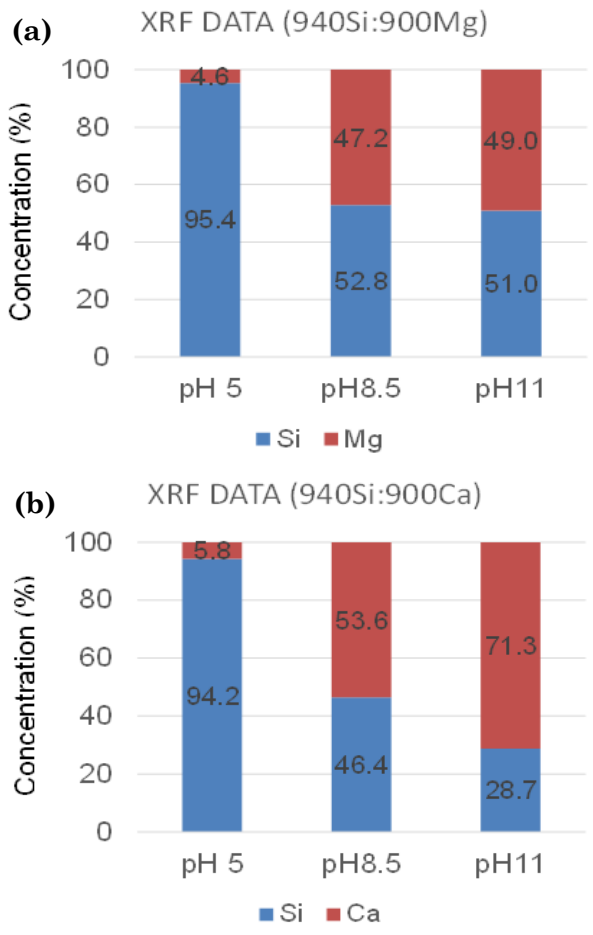

Figure 10. The element concentration analysed by XRF for (a) Si/Mg and (b) Si/Ca at various pH conditions

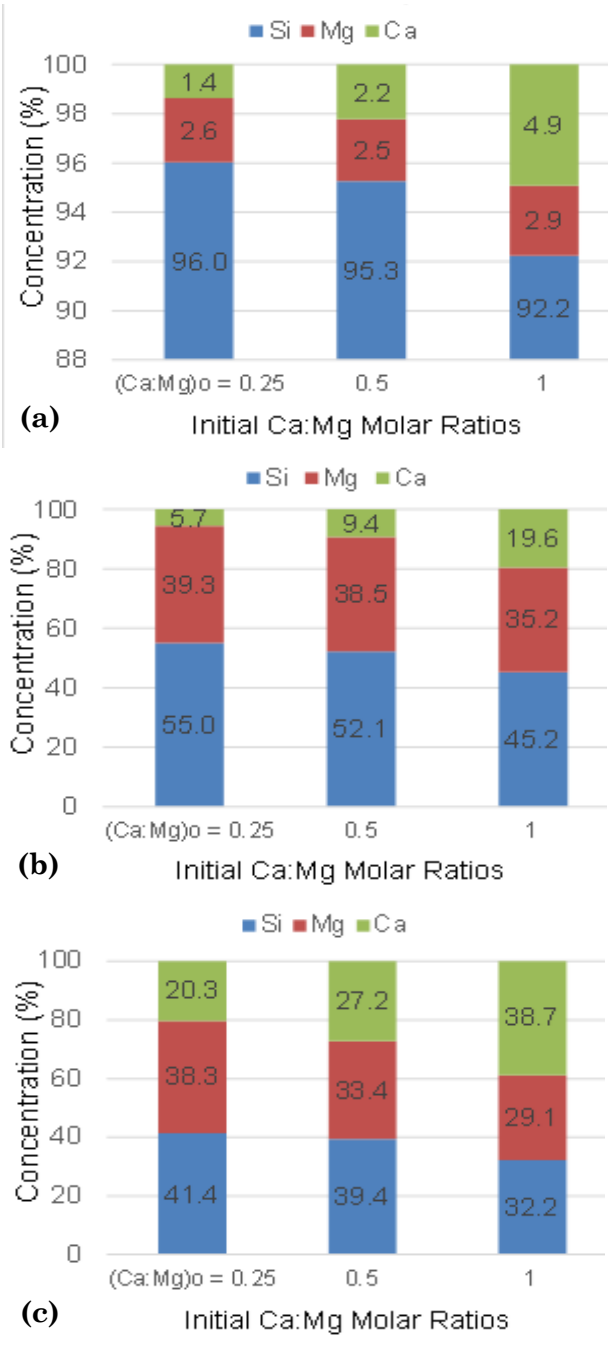

Figure 11. The element concentration analysed by XRF for various $(Ca:Mg)_o$ at various pH: (a) pH 5, (b) pH 8.5 and (c) pH 11.

phous colloidal silica in which the percentage of Si varied from 96% at pH 5 and gradually reduce to 95.3% and 92.2% at pH 8.5 and pH 11, shown in Figure 11(b) and 11(c), respectively. At pH 8.5 (Figure 11(b)), the percentage of Mg present in the precipitate increased significantly from 2.6–2.9 % to 35.2–39.3 %. This is in agreement with the AAS results in Figure 8, where magnesium silicate is very likely to form at higher pH due to the reactive silicate ions formed. The XRF data in Figure 11 shows the decrease in the percentage of silica and contrasts with the increase in the percentage of calcium as the pH increases from pH 5 to pH 11. This XRF data complements the AAS analysis and confirms that the silica has a higher tendency to bridge the Mg ion than the Ca ion, and also silica reacts with more Ca ion at high Ca concentration and at higher pH.

At high temperature (in this case 90 °C) and high Ca concentration (relative to Mg ion), Ca ions have a high tendency to bridge the Si backbone. Hauksson *et al.* [27] reports that commonly encountered cations affect solubility in the order of Mg > Ca > Sr > Li> Na > K.

3.4 FTIR Results and Analysis: Materials and Functional Groups Identification

To confirm the presence of amorphous/crystalline of silica/silicate scale, the precipitates were characterized using FTIR analysis to identify the functional groups that were present.

3.4.1 FTIR of precipitates in Si-containing only brine

Referring to Figure 12, at low pH (pH 5), FTIR bands around 1070 cm^{-1} and ~970 cm^{-1} was observed which showed the Si–O–Si, and Si–OH asymmetric stretching modes, respectively, which is consistent with previously reported studies by Sazali [22], Sazali *et al.* [23], El Nahrawy *et al.* [29], and Joni *et al.* [30]. The presence of a broad and strong band around 3440 cm^{-1} is evidence for the existence of a stretching vibration of hydroxyl groups (Si–OH) in the structure of SiO_2 [29,31]. According to Musić *et al.* [31], the FTIR band around 1632 cm^{-1} is due to the bending vibration of H_2O molecules while the 785 cm^{-1} can be assigned to a Si–O–Si symmetric stretching vibration [31]. All of the bands shown for the pH 5 condition resemble the formation of silica SiO_2 which is consistent with the observation seen in Figure 2. In Figure 2, the Si-containing only brine shows that the solution turned cloudy solution after 22 h at pH 5 and more was observed for the concentrated Si brine, 1880 ppm (as compared to 940 ppm).

These five bands absent in the spectra recorded for the basic conditions, *i.e.* pH 8.5 and pH 11 and this is consistent with the observation shown in Figure 2 where the Si brine under basic pH remained clear, even after 22 h of reaction. However, this must be proved via the ICP analysis to determine the extent of the reaction of Si for this basic condition. The spectra bands actually observed agreed well with Alexander *et al.* results [32] which stated that the solubility of the amorphous silica increased

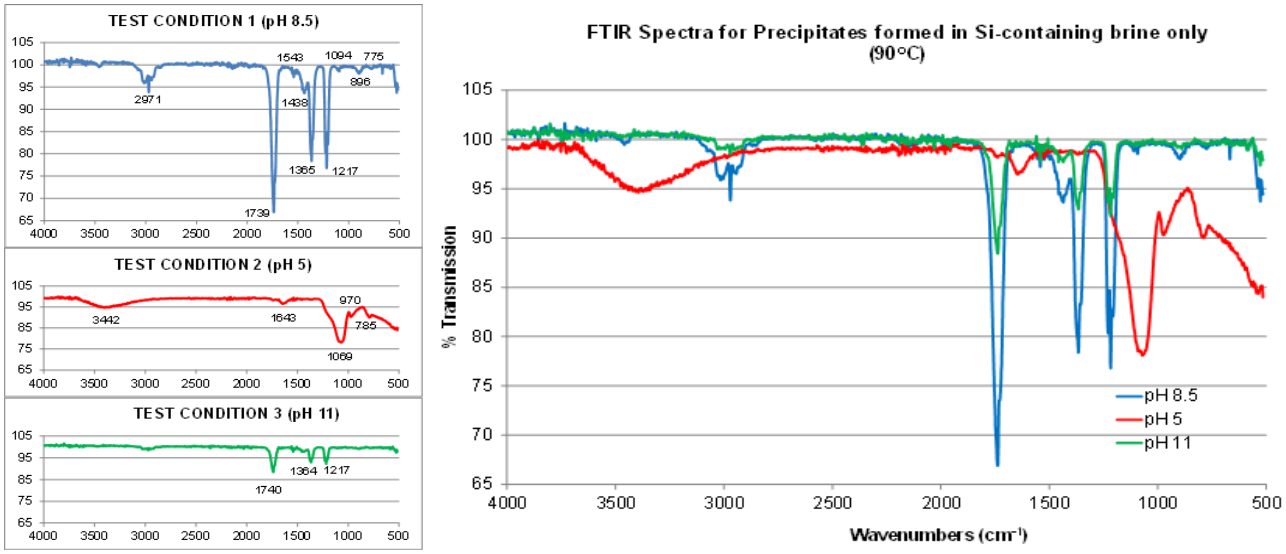

Figure 12. FTIR spectra for precipitate formed from Si-containing only brine, 1880 ppm Si at various pH conditions (temperature 90 °C).

with a pH increase. In addition, it has been stated by Osswald & Fehr [33] that solid silica gels commonly have 4 peaks at ~1200 cm^{-1}, ~1150 cm^{-1}, ~1100 cm^{-1}, and ~950 cm^{-1} relating to the Si–O–Si asymmetric stretching vibration, skeletal Si–O stretching vibration, Si–O–Si asymmetric stretching vibration, and Si–O stretching vibration of surface silanol groups, respectively as illustrated in Figure 12 [33]. The band ~1217 cm^{-1} observed for both basic conditions may be due to the Si–O–Si asymmetric stretching vibration [33,34]. If the FTIR spectra at pH 8.5 is examined carefully, weaker peaks can be observed for the Si–O–Si bond at 1094 cm^{-1}, the Si–OH bond at 896 cm^{-1}, and the Si–O–Si symmetric stretching vibration at 775 cm^{-1} [29,34]. These weaker peaks were not observed at the higher pH 11 conditions. Considering all these observations, it can be concluded that the Si-brine only may produce very small amount of silica under the basic conditions, however, due to its high stability, it is less likely to be stable and be observed.

3.4.2 FTIR of precipitates in Si/Mg mixed brine

Sazali [22] analysed the FTIR spectra of the commercial magnesium silicate scale $MgSiO_3$ showing the important peaks at ~1014 cm^{-1}, ~789 cm^{-1}, and ~675 cm^{-1} may be assigned to the Si–O–Si symmetrical stretching vibration, Si–O–Si symmetric, and Si–O bending motion respectively which agreed well with results of Rashid *et al.* [35]. Jäger *et al.* [36] also concluded that the position of the Si–O stretching vibration is shifted from ~1111 cm^{-1} (9 μm) for the pure SiO_2 to ~1030 cm^{-1} (9.7 μm) for $MgSiO_3$ and to ~975 cm^{-1} (10.25 μm) for $Mg_{2.4}SiO_{4.4}$ [36].

With reference to Figure 13, the precipitates at pH 8.5 showed peaks at 1000 cm^{-1}, 898 cm^{-1}, and 635 cm^{-1} that may refer to Si–O stretching vibration for Mg-silicate; Si–O band; and Si–O bending motion. These 3 bands were further shifted to the right for precipitates formed at the higher pH 11, *i.e.* at 980 cm^{-1}, 887 cm^{-1}, and 610 cm^{-1}, respectively. The band at ~1217 cm^{-1} observed for the Si-only brine due to the Si–O–Si asymmetric stretching vibration was also observed for both basic conditions.

When closely examined, two peaks at 1435 cm^{-1} and 1365 cm^{-1} were observed in for the basic conditions and may refer to overtone combination bands and water bending modes such as H–O–H, Si–O–H, or Mg–O–H [37]. Hofmeister and Bowey [37] reported overtone combination bands and water bending modes such as H–O–H, Si–O–H or Mg–O–H (all near 5–8 μm/ 2000–1250 cm^{-1}), whereas Jiang *et al.* [38] reported a bending vibration of OH bond at ~1456 cm^{-1} when they analysed $Mg(OH)_2$. Under acidic conditions, the precipitates exhibited a very strong and broad peak at ~1100 cm^{-1} which is usually assigned to the transverse optical mode (TO) and longitudinal optical mode (LO) of the Si–O–Si asymmetric stretching vibration, ~957 cm^{-1} due to the silanol group and ~794 cm^{-1} due to Si–O–Si symmetric stretching vibration [31,37].

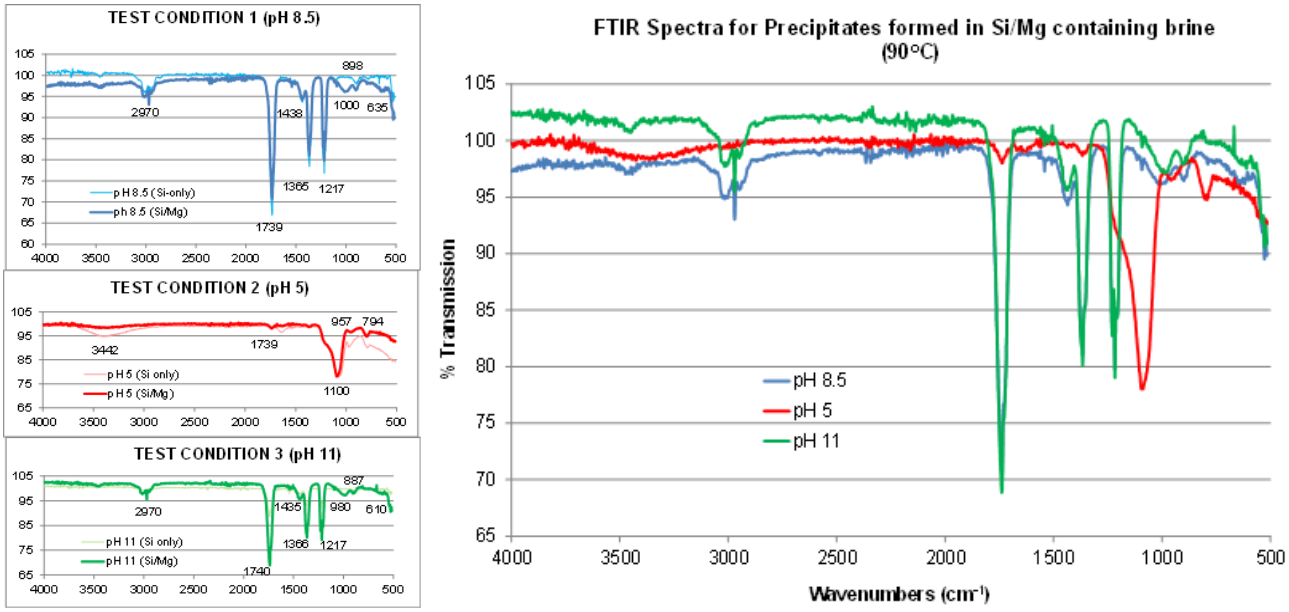

Figure 13. FTIR spectra for precipitate formed from Si/Mg mixed brine, 940Si:900Mg at various pH (temperature 90 °C).

Through detailed analysis of the FTIR spectra, the precipitates formed at pH 8.5 and pH 11 may consist of a mixed scale, *i.e.* amorphous silica, amorphous magnesium silicate, and magnesium hydroxide. The magnesium silicate produced at both pH values may differ structurally, as the peaks at 1000 cm^{-1} (~980 cm^{-1} at pH 11) and 898 cm^{-1} (~887 cm^{-1} at pH 11) and 635 cm^{-1} (610 cm^{-1} at pH 11) have been shifted further (to the right) for the higher pH 11. This may indicate a different stoichiometric ratio of MgO to SiO. Also, the peaks observed at ~1430 cm^{-1} may indicate to some extent, a little amount of $Mg(OH)_2$ may form in both basic environments.

The main precipitate produced in the acidic conditions is mainly amorphous silica scale, however, the AAS analysis showed that a significant amount of reacted Mg. Jäger *et al.* [36] reported that the position of the Si–O stretching vibration is shifted from 9 µm (1111.1 cm^{-1}) for pure SiO_2 to 9.7 µm (1030.9 cm^{-1}) for $MgSiO_3$ and 10.25 µm (975.6 cm^{-1}) for $Mg_{2.4}SiO_{4.4}$. Hence, it is believed that Mg-silicate may also have formed with a higher ratio of Mg^{2+} ions bridges to the SiO_2 backbone (as compared to the SiO_2 back bone under the basic condition) as a peak at ~957 cm^{-1} was observed for the acidic condition.

3.4.3 FTIR of precipitates in Si/Ca mixed brine

Based on Figure 14, for Test Condition 1, a broad band ~3408 cm^{-1} was observed that is due to the moisture absorption band [39]. A peak at ~1455 cm^{-1} was also seen in this pH 8.5 solution that may indicate the presence of a Ca–O functional group due to CaO or Ca(OH) which agreed with Galván-Ruiz *et al.* [40]. Peaks at ~1068 cm^{-1} and ~829 cm^{-1} may indicate Si–O–Si, Si–O–Ca asymmetric stretching modes. El Nahrawy *et al.* [29] reported these functional groups *i.e.* Si–O–Si, Si–O–Ca asymmetric stretching mode at ~1075 cm^{-1} whereas Husain *et al.* [41] reported Si–O–Ca asymmetric stretching modes may be seen at ~848 cm^{-1} and ~999–1001 cm^{-1} [29,41]. A peak at ~965 cm^{-1} may be due to Si–OH, Ca–OH asymmetric stretching modes [29] or Si–O stretching modes [39]. The precipitate formed at pH 8.5 at ~791 cm^{-1} that may indicate the presence of SiO_2 [40]. Galván-Ruiz *et al.* [40] also reported that FTIR spectra bands were observed at 3643, 1417, 866 cm^{-1} for Ca(O) and 3643, 2500, 1427, 875, and 500 cm^{-1} for $Ca(OH)_2$ [40]. Based on this detailed inspection of all the peaks, it is postulated that the precipitates formed at pH 8.5 may be a combination of mostly silica SiO_2, Ca-silicate scale, and a little fraction of $Ca(OH)_2$. As for the precipitates formed at acidic pH 5, peaks were observed at 1092 cm^{-1}; 952 cm^{-1}; and 793 cm^{-1} possibly indicating the presence of Si–O–Si, Si–O–Ca asymmetric stretching mode; silanol group; and Si–O–Si symmetric stretching vibration; respectively. Hence, the most probable scale produced may be a mixed scale of silica and Ca-silicate scale.

Precipitates at the higher pH 11 value show bands at ~1458 cm^{-1} (Ca–O), ~1061 cm^{-1} (Si–O–Si, Si–O–Ca), and ~853 cm^{-1} ($CaO/Ca(OH)_2$) indicating the presence of amorphous silica SiO_2, Ca-silicate scale, and

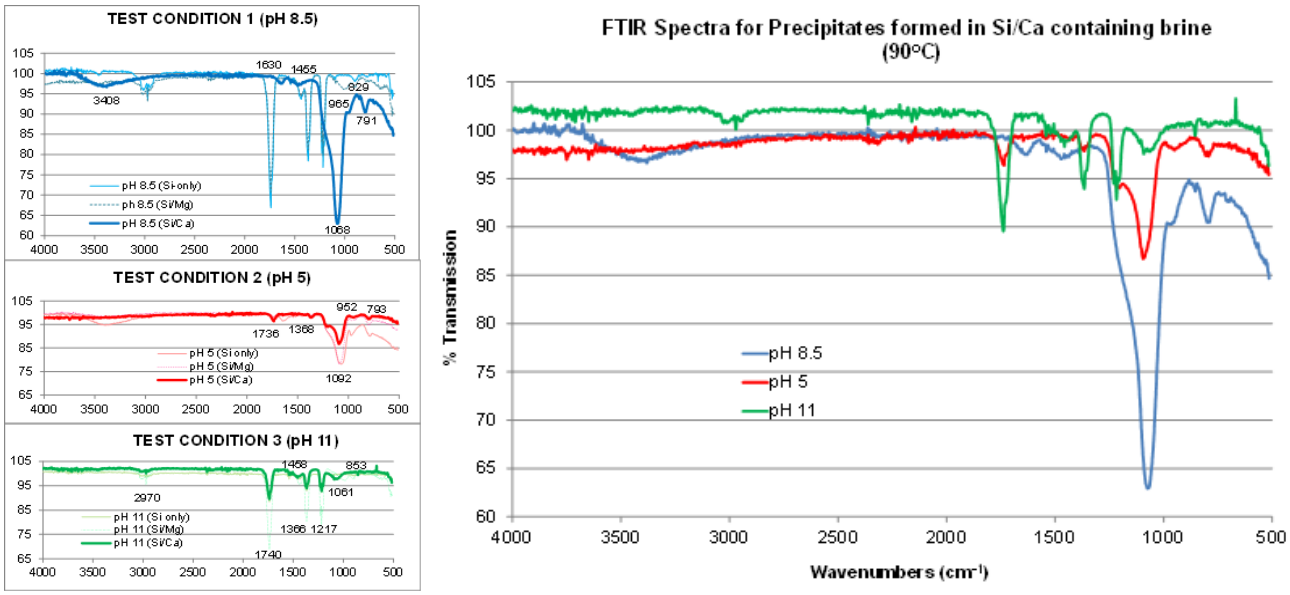

Figure 14. FTIR spectra for precipitate formed from Si/Ca mixed brine, 940Si:900Ca at various pHs (& 90 °C).

$Ca(OH)_2$. It is postulated that more Ca-silicate and $Ca(OH)_2$ formed at pH 11 due to the higher pH environment and the AAS results shows more than 90 % of Ca^{2+} ions reacted even after only 2 h of reaction. The morphologies of all the scales formed may be crystalline or amorphous, though this may need to be reconfirmed by XRD.

3.4.4 FTIR of precipitates in Si/Mg/Ca mixed brine with various initial molar concentrations of Ca to Mg at various pH values

Generally, the FTIR spectra for both basic conditions are similar with bands observed at ~1000 cm^{-1}, ~791 cm^{-1}, and ~651 cm^{-1} that may indicate the presence of Mg-silicate, Ca-silicate scale, or even Mg-Ca-silicate scale (Figure 15). However, no band appeared at ~1458 cm^{-1} for precipitates formed at pH 8.5. AAS revealed that ~95% and ~82% of Mg and Ca ions reacted at pH 8.5 as opposed to almost 100% of both ions reacting at pH 11. Hence, the ~1458 cm^{-1} band seen in precipitates formed at pH 11 may indicate the presence of $Mg(OH)_2$ and $Ca(OH)_2$ scale in addition to the aforementioned scale.

In contrast, the spectra of the precipitates at pH 5 show similar bands at ~1739 cm^{-1}, ~1367 cm^{-1}, ~1217 cm^{-1} as observed for both basic environments. However, the band around 1000 cm^{-1} was further to the left, at around ~1090 cm^{-1}. AAS reported that only ~35% of Mg ions reacted as opposed to ~82% of Ca for the acidic environment. This was probably due to unionized silica at this low pH, which resulted in less Mg ion bridged into the silica backbone. Silica polymerization rapidly occurred due to the high temperature and Ca ions dominantly bridging the silica backbone in this low pH environment. It is postulated that precipi-

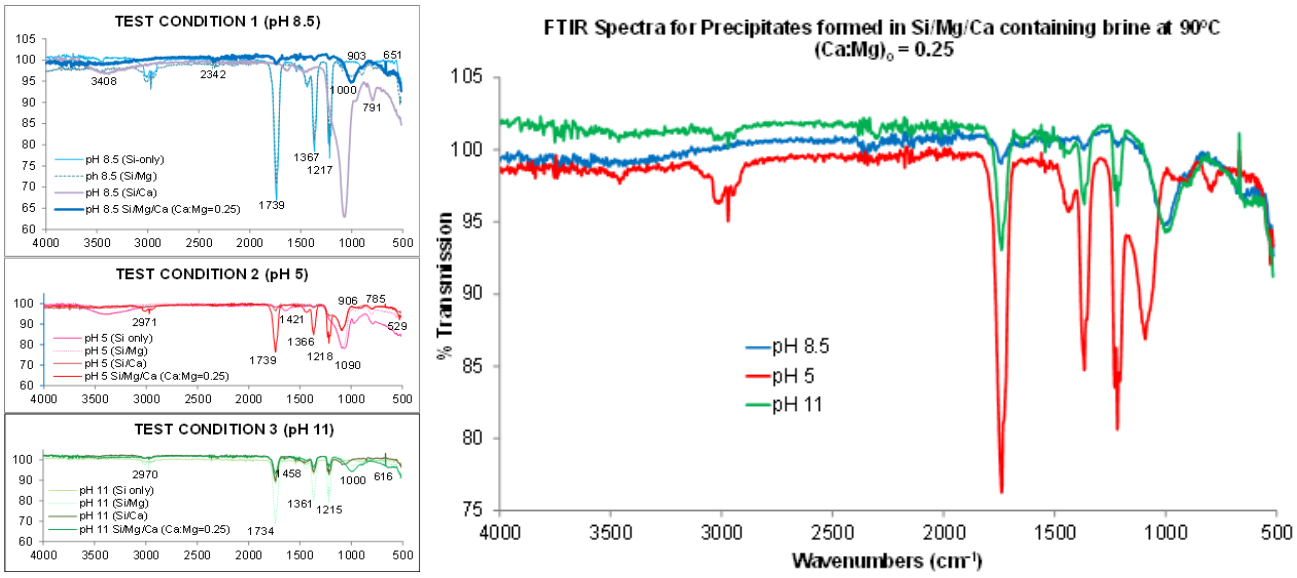

Figure 15. FTIR spectra for precipitate formed from Si/Mg/Ca mixed brine (Ca:Mg)o = 0.25 at various pH conditions.

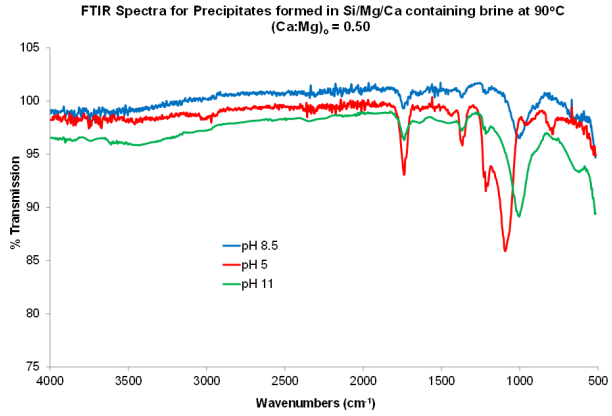

Figure 16. FTIR spectra for precipitate formed from Si/Mg/Ca mixed brine (Ca:Mg)o=0.5 at various pH conditions.

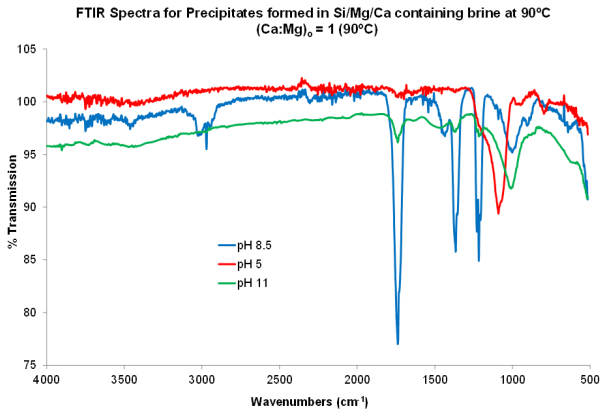

Figure 17. FTIR spectra for precipitate formed from Si/Mg/Ca mixed brine(Ca:Mg)o=1 at various pH conditions.

tates formed were a mix of silica, Mg-silicate, Ca-silicate, and Mg-Ca-silicate scale.

Figures 16 and 17 shows the FTIR bands for initial calcium to magnesium molar ratios of 0.5 and 1.0, respectively at various pH values. The same trends were observed for all Ca:Mg molar ratios, with a peak at ~1000 cm^{-1} for both pH 8.5 and pH 11. However, the peak at around 650 cm^{-1} for pH 8.5 was shifted to the right to ~616 cm^{-1} in the precipitates formed at the higher pH 11, this trend was observed for all Ca:Mg molar ratios. Figures 15, 16, and 17 were examined and peaks at ~1734 cm^{-1}, ~1361 cm^{-1}, and ~1215 cm^{-1} were observed in all Ca:Mg molar ratios for the basic environment and acidic pH 5, except for initial molar ratio Ca:Mg of 1. Figure 17 shows the band at ~1734 cm^{-1} was very weak; ~1364 cm^{-1} was almost gone; and no band was detected at ~1215 cm^{-1}, for this $(Ca:Mg)_o$ of 1 at pH 5. In addition, it was found that peaks at ~1090 cm^{-1} and ~790 cm^{-1} appeared for all molar ratios. As the initial amount of Ca ions increased, it was found that the band at ~900 cm^{-1} (at $(Ca:Mg)_o$ = 0.25) was shifted to ~950 cm^{-1} (at $(Ca:Mg)_o$ = 0.5 and 1.0).

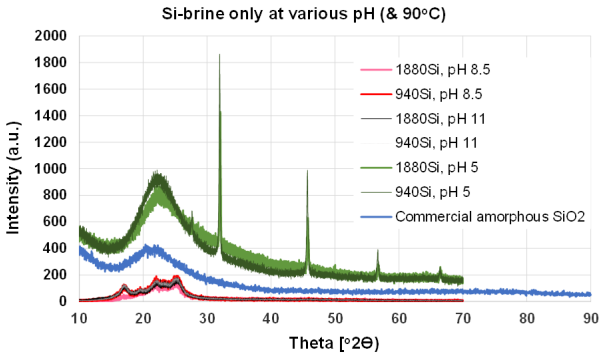

Figure 18. XRD pattern for Si-only containing brine of 1880ppm/940ppm Si at various pH conditions.

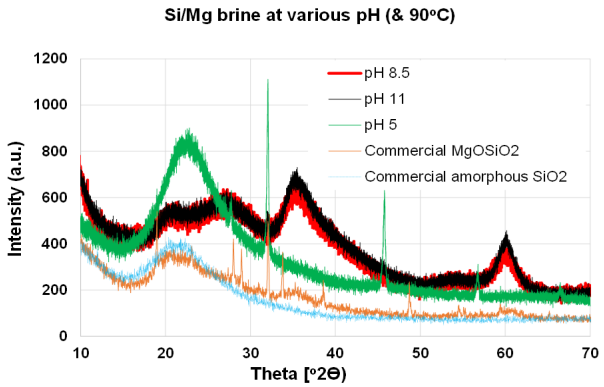

Figure 19. XRD pattern for Si/Mg brine of 940Si:900Mg at various pH conditions.

3.5 XRD Results and Analysis: Crystallographic Structure of the Silica/ Silicate Scale

3.5.1 XRD diffraction pattern for Si-containing only brine

Based on Figure 18 showing the XRD pattern for Si-containing only brine, it was observed the broad peaks between the range of 17° to 26° belonged to the amorphous silica, which agreed well with XRD patterns of commercial amorphous silica as previously reported by Sazali [22]. This may be due to the reduced solubility of silica which leads to the polymerization of silicic acid. At pH 5, amorphous silica not only detected with broad peaks at 23°, but also crystalline silica (may be microcrystalline) was observed with the sharp peaks at theta of 32°, 46°, 56° and 66°, due to the high test temperature of 90 °C.

3.5.2 XRD diffraction pattern for Si/Mg mixed brine

Figure 19 shows the diffraction pattern results for precipitate formed under basic pH conditions resembles the commercial amorphous magnesium silicate analysed by Sazali [22]. It show the broad peaks indicating the amorphous silica (~ 23°) and amorphous magnesium silicate (a broad peak from ~33° to ~40° and small hump at ~60°) exists [22]. In contrast, the precipitates that were formed in acidic pH resemble the amorphous silica except with sharp peaks (that may indicate microcrystalline silica also co-existed) exist at the same position observed in Si-brine only (but with lower intensity), in addition to the broad amorphous silica peak at 23°.

3.5.3 XRD diffraction pattern for Si/Ca mixed brine

Figure 20 shows at low pH 5, the precipitation resembled silica which is mostly amor-

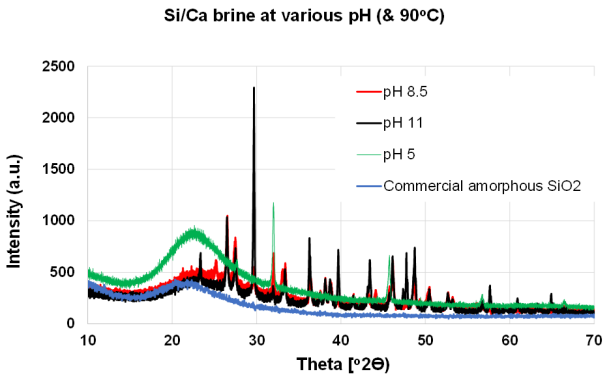

Figure 20. XRD pattern for Si/Ca brine of 940Si:900Ca at various pH conditions.

phous form shown by the peak presence at 23°, with 4 sharp peaks at ~32°, ~46°, ~56°, and ~66° indicating a microcrystalline precipitate co-existed. It was different at higher pH 8.5 and pH 11, where the sharp peaks appeared at many theta values indicating the crystalline Ca-silicate may have dominated in the precipitates formed. The broad peak at ~23° became less obvious (though this may indicate amorphous silica was also formed) indicating more calcium ions bridged the silica backbone and produced a microcrystalline Ca-silicate scale. These observations revealed that the presence of calcium ions in the silica scaling environment shifted the silica type from an amorphous silica scale to a mixture of amorphous silica and crystalline Ca-silicate scale in a basic pH environment which agreed with observations by Sazali *et al.* [42]. Also, the presence of Ca ion may already produce a microcrystalline silica scale even at low pH conditions.

3.5.4 XRD diffraction pattern for Si/Mg/Ca mixed brine

The XRD data for the diffraction pattern of precipitate formed at different initial calcium concentrations present in the mixed brine are shown in Figures 21, 22, and 23. Precipitates formed in all $(Ca:Mg)_o$ molar ratios at low pH 5 exhibit the presence of amorphous silica with broad peaks at 23° and sharp peaks appearing at ~32°, ~46°, ~56°, and ~66°, with increased intensity with an increase of calcium ions present. For the precipitates formed at the lowest $(Ca:Mg)_o$ = 0.25 for pH 8.5, the precipitation formed appeared to resemble a mixture of amorphous silica (as the same broad peak at ~23° was seen) and amorphous magnesium silicate (as humps at ~28°, ~36°, ~54°, ~60° were seen). However, as the amount of calcium ions increased, the same broad peaks/humps appeared except the hump at ~54°. In addition, several sharp peaks were seen at ~30°, ~36°, ~40°, ~43°, ~47°, ~48°, ~51° for $(Ca:Mg)_o$ = 0.5; and ~23°, ~30°, ~36°, ~40°, ~43°, ~47°, ~48°, ~57°, and ~58° for $(Ca:Mg)_o$ = 1.

Finally, for the precipitates formed at the highest pH 11 value, all peaks detected showed multiple sharp peaks at various positions, with the number of sharp peaks increased as the number of calcium ions present in the scaling brine were increased. The XRD results shown may conclude that as the number of calcium ions present in the Si/Mg/Ca scaling brine increase, the more crystalline the precipitates is formed.

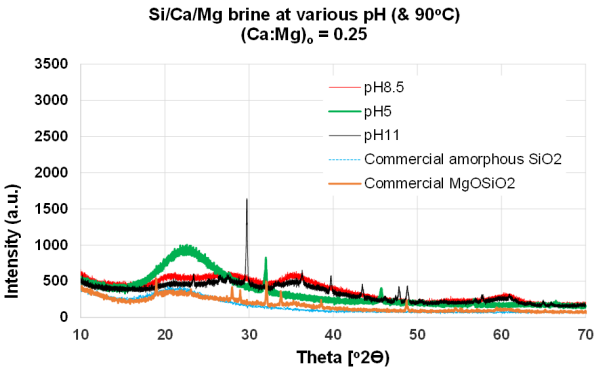

Figure 21. XRD pattern for Si/Mg/Ca brine of 940Si:450Mg:187.5Ca at various pH conditions.

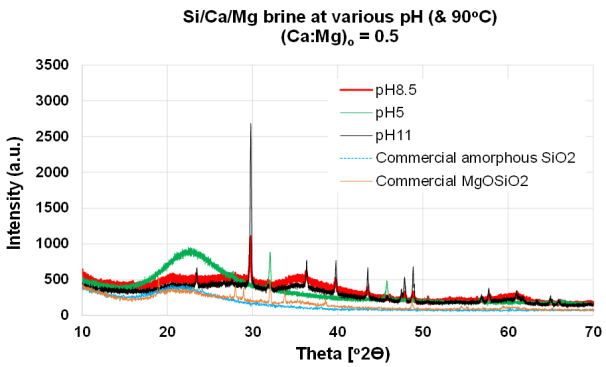

Figure 22. XRD pattern for Si/Mg/Ca brine of 940Si:450Mg:375Ca at various pH conditions.

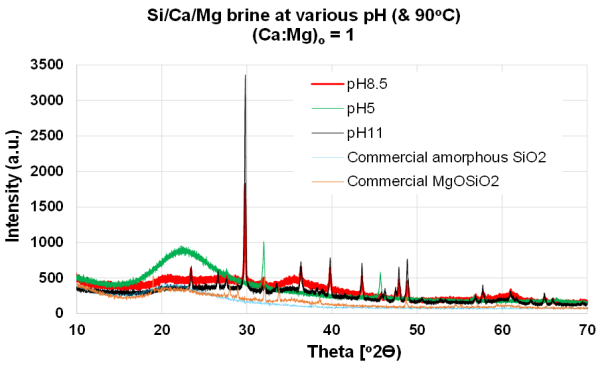

Figure 23. XRD pattern for Si/Mg/Ca brine of 940Si:450Mg:750Ca at various pH conditions.

3.6 Scanning Electron Microscope / Energy Dispersive X-ray Spectroscopy (SEM/EDAX) – Surface Topography

The types and morphology of silicate scale formed under different pH conditions was verified by the analysis data of SEM/EDAX on the collected precipitate. Based on the SEM images in Figure 24, it was demonstrated that for both basic conditions, the solid silicate scales formed were amorphous in nature with a small amount of microcrystalline. The main elements in the precipitates were found to be Oxygen

33.0 weight% (wt%), Magnesium (21.9 wt%), and Silicon of 37.1 wt% with traces of sodium and chloride for precipitates formed at pH 8.5 as shown in Table 5. As for the precipitates formed at pH 11, they consisted of Oxygen (26.5 wt%), Magnesium (23.5 wt%), and Silicon (44.6 wt%). The precipitates for the acidic conditions appeared to be crystalline silica in nature.

Based on the SEM images in Figure 25, the precipitates formed in a higher calcium ion environment produced a much smaller particle size. The precipitates formed for this silicate scale consisted of Magnesium (11.5 to 14.3%), Silicon (39.7 to 50.4%), Oxygen (24.1 to 36.6%), and Calcium (5.3 to 8.1%) with traces of sodium and chloride.

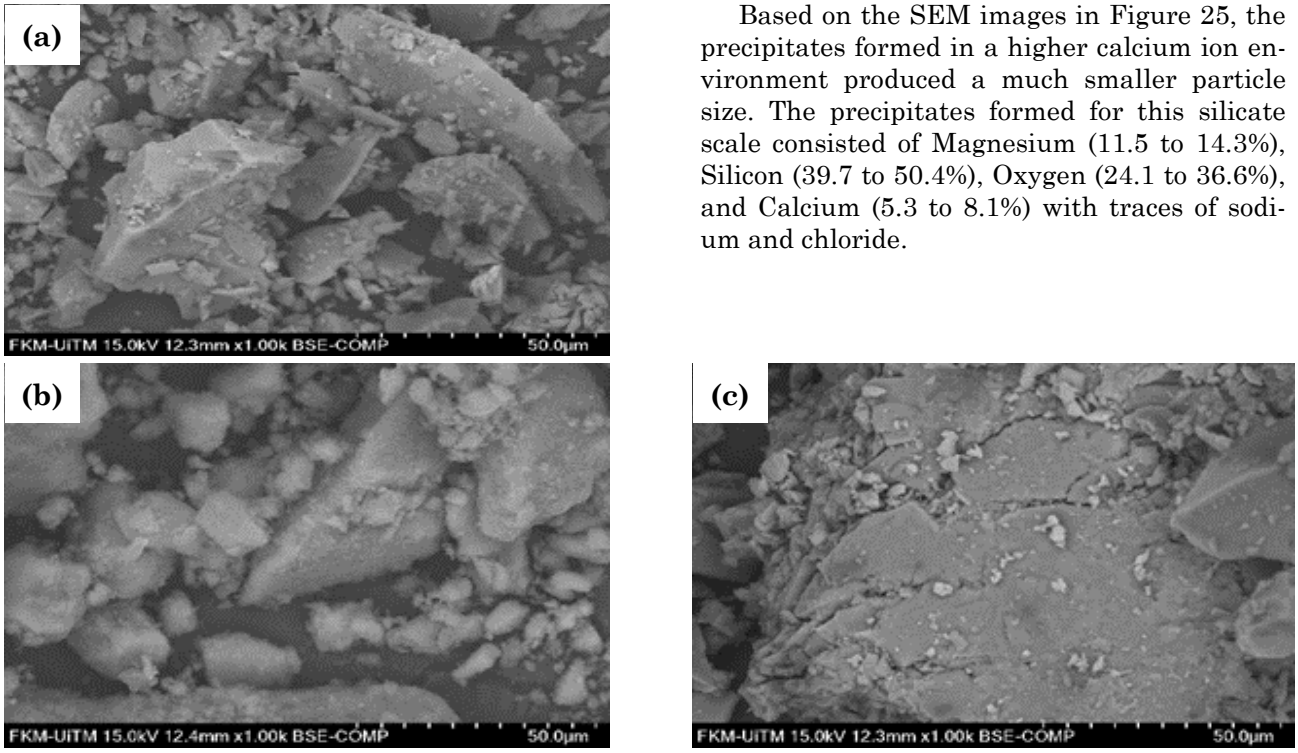

Figure 24. SEM image for precipitate formed from mixing solution of 940Si:900Mg in (a) Test condition 1 (b) Test condition 2 and (c) Test condition 3.

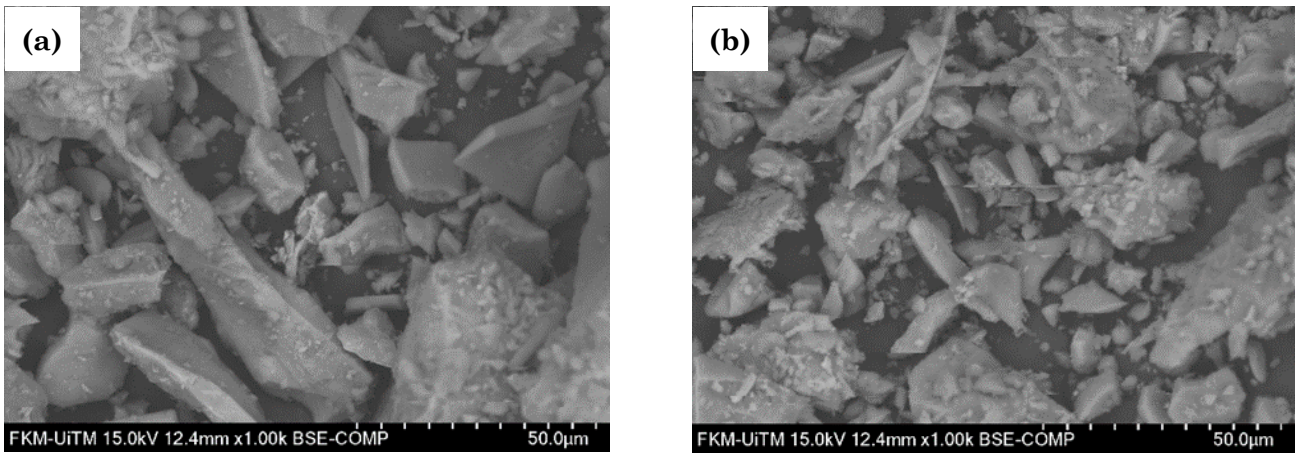

Figure 25. SEM image for precipitate formed in various initial Ca concentrations; 940Si:900Mg with (a) 375 ppm Ca and (b) 750 ppm Ca at pH 8.5.

Table 5. Weight% for SEM/EDAX spectrum of the precipitates in various tested conditions.

No. sample	Weight %			
	Magnesium (Mg)	Silicon (Si)	Oxygen (O)	Calcium (Ca)
Si/Mg at pH 8.5	21.9	37.1	33	-
Si/Mg at pH 5	-	64.7	35.3	-
Si/Mg at pH 11	23.5	44.6	26.5	-
Si/Mg/Ca $(Ca:Mg)_o = 0.5$ at pH 8.5	14.3	50.4	24.1	5.3
Si/Mg/Ca $(Ca:Mg)_o = 1$ at pH 8.5	11.5	39.7	36.6	8.1

4. Conclusions

To conclude, pH plays a major role in silicate scaling. Different amounts of magnesium ion reacted, $[Mg]_{rx}$ and calcium ion reacted, $[Ca]_{rx}$ calculated from the AAS analysis indicated that different compounds were produced in the precipitates formed under different pH conditions. These conjectures are supported by the peak differences in FTIR spectra produced for the precipitates under different pH conditions. The presence of calcium ions (and various $(Ca:Mg)_o$) was found to significantly affect the type and morphology of the scale produced (sharp peaks observed in the XRD related to microcrystalline structures) as well as the severity of the scaling reaction. The morphology of precipitates formed under all pH conditions was generally amorphous in nature with a small amount of microcrystalline/crystalline forms that had co-produced throughout the scaling reaction.

Acknowledgment

This work is supported by the Ministry of Higher Education (MOHE) Malaysia and Universiti Teknologi MARA (UiTM), under the Fundamental Research Grant Scheme (UiTM reference no: 600-IRMI/FRGS 5/3 (411/2019) & MyGrant reference code: FRGS/1/2019/TK07/UITM/02/10). A special thanks to the laboratory staff of the Flow Assurance and Scale Team, Institute of GeoEnergy Engineering, Heriot-Watt University, United Kingdom & College of Engineering, Universiti Teknologi MARA for the facilities, help, and assistance given to complete this study.

References

[1] Kumar, A., Mandal, A. (2017). Synthesis and Physiochemical Characterization of Zwitterionic Surfactant for Application in Enhanced Oil Recovery. *Journal of Molecular Liquids*, 243, 61–71. DOI: 10.1016/j.molliq.2017.08.032.

[2] Wu, F., Hou, J., Wang, Z., Ma, Y., Wang, D. (2018). An Enhanced Oil Recovery Technique by Targeted Delivery ASP Flooding. *Petroleum Exploration and Development*, 45(2), 321–327. DOI: 10.1016/S1876-3804(18)30035-1.

[3] Saha, R., Uppaluri, R.V.S., Tiwari, P. (2018). Influence of Emulsification, Interfacial Tension, Wettability Alteration and Saponification on Residual Oil Recovery by Alkali Flooding. *Journal of Industrial and Engineering Chemistry*, 59, 286–296. DOI: 10.1016/j.jiec.2017.10.034.

[4] Wu, Y., Chen, W., Dai, C., Huang, Y., Li, H., Zhao, M., He, L., Jiao, B. (2017). Reducing Surfactant Adsorption on Rock by Silica Nanoparticles for Enhanced Oil Recovery. *Journal of Petroleum Science and Engineering*, 153, 283–287. DOI: 10.1016/j.petrol.2017.04.015.

[5] Al-Hajri, S., Mahmood, S.M., Abdulelah, H., Akbari, S. (2018). An Overview on Polymer Retention in Porous Media. *Energies*, 11(10), 2751–2769. DOI: 10.3390/en11102751.

[6] Gbadamosi, A.O., Junin, R., Manan, M.A., Agi, A., Yusuff, A.S. (2019). An Overview of Chemical Enhanced Oil Recovery: Recent Advances and Prospects. *International Nano Letters*, 9(3), 171–202. DOI: 10.1007/s40089-019-0272-8.

[7] Jiecheng, C., Wanfu, Z., Yusheng, Z., Guangtian, X., Chengfeng, R., Zhangang, P., Wenguang, B., Zongyu, Z., Xin, W., Hairong, F., Qingguo, W., Xianxiao, K., Lei, S. (2011). Scaling Principle and Scaling Prediction in ASP Flooding Producers in Daqing Oilfield. In: *SPE Enhanced Oil Recovery Conference*. Kuala Lumpur: Society of Petroleum Engineer, pp. 19–21. DOI: 10.2118/144826-MS.

[8] Umar, A.A., Saaid, I.B.M. (2013). Silicate Scales Formation during ASP Flooding: A Review. *Research Journal of Applied Sciences, Engineering and Technology*, 6(9), 1543–1555. DOI: 10.19026/rjaset.6.3867.

[9] Guo, H., Li, Y., Wang, F., Yu, Z., Chen, Z., Wang, Y., Gao, X. (2017). ASP Flooding: Theory and Practice Progress in China. *Journal of Chemistry*, 2017, 8509563. DOI: 10.1155/2017/8509563.

[10] Brown, K. (2011). Thermodynamics and Kinetics of Silica Scaling. In: *Proceedings International Workshop on Mineral Scaling*. Manila.

[11] Fournier, R.O., Rowe, J.J. (1977). The Solubility of Amorphous Silica in Water at High Temperatures and High Pressures. *American Mineralogist*, 62(9–10), 1052–1056.

[12] Helgeson, H.C. (1969). Thermodynamics of Hydrothermal Systems at Elevated Temperatures and Pressures. *American Journal of Science*, 267(7), 729–804. DOI: 10.2475/ajs.267.7.729.

[13] Henley, R.W. (1983). pH and Silica Scaling Control in Geothermal Field Development. *Geothermics*, 12(4), 307–321. DOI: 10.1016/0375-6505(83)90004-4.

[14] van den Heuvel, D.B., Gunnlaugsson, E., Gunnarsson, I., Stawski, T.M., Peacock, C.L., Benning, L.G. (2018). Understanding Amorphous Silica Scaling Under Well-Constrained Conditions inside Geothermal Pipelines. *Geothermics*, 76(2018), 231–241. DOI: 10.1016/j.geothermics.2018.07.006.

[15] Mahat, S.Q.A., Saaid, I.M., Lal, B. (2016). Green Silica Scale Inhibitors for Alkaline-Surfactant-Polymer Flooding: A Review. *Journal of Petroleum Exploration and Production Technology*, 6(3), 379–385. DOI: 10.1007/s13202-015-0187-5.

[16] Meyers, P. (1999). Behavior of Silica in Ion Exchange and Other Systems. In: *The International Water Conference: 60th Annual Meeting*. Pittsburgh:, pp. 492–501.

[17] Qing, J., Bin, Z., Ronglan, Z., Zhongxi, C., Zhou, Y. (2002). Development and Application of a Silicate Scale Inhibitor for ASP Flooding Production Scale. In: *International Symposium Oilfield Scale*. Aberdeen: United Kingdom, January 2002. DOI: 10.2118/74675-ms.

[18] Fleming, B.A., Crerari, D.A. (1982). Silicic Acid Ionization and Calculation of Silica Solubility at Elevated Temperature and pH Application to Geothermal Fluid Processing and Reinjection. *Geothermics*, 11(1), 15–29. DOI: 10.1016/0375-6505(82)90004-9.

[19] Kashpura, V.N., Potapov, V.V. (2000). Study of the Amorphous Silica Scales Formation at the Mutnovskoe Hydrothermal Field (Russia). In: *PROCEEDINGS, Twenty-Fifth Workshop on Geothermal Reservoir Engineering*. California.

[20] Lu, H., Brooks, J., Legan, R., Fritz, S. (2018). Novel Laboratory Test Method and Field Applications for Silica/Silicate and Other Problematic Scale Control. In: *SPE International Oilfield Scale Conference and Exhibition*. Aberdeen. DOI: 10.2118/190705-MS.

[21] Wang, W., Wei, W. (2016). Silica and Silicate Scale Formation and Control: Scale Modeling, Lab Testing, Scale Characterization, and Field Observation. In: *SPE International Oilfield Scale Conference and Exhibition*. Aberdeen: SPE. DOI: 10.2118/179897-MS.

[22] Sazali, R.A. (2018). The Development of A Test Methodology and New Findings in Silicate Scale Formation and Inhibition. *PhD Thesis*, Institute of Petroleum Engineering School of Energy, Geoscience, Infrastructure & Society, Heriot Watt University, United Kingdom.

[23] Sazali, R.A., Sorbie, K.S., Boak, L.S. (2015). The Effect of pH on Silicate Scaling. In: *SPE - European Formation Damage Conference, Proceedings, EFDC*. Budapest: Society of Petroleum Engineers (SPE), pp. 316–328. DOI: 10.2118/174193-ms.

[24] Cowan, J.C., Weintritt, D.J. (1976). Water Formed Scale Deposits. In: Gulf Publishing Company. https://scholar.google.com/scholar?hl=en&as_sdt=0%2C5&q=Water+Formed+Scale+Deposits+Cowan%2C+J.+C.+and+Weintritt%2C+D.+J.+%28Eds.%29.+&btnG=. Accessed 9 Sep 2022.

[25] Iler, R.K. (1979). *The Chemistry of Silica: Solubility, Polymerization, Colloid and Surface Properties, and Biochemistry*. John Wiley & Sons.

[26] MacAdam, J., Jarvis, P. (2015). Water-Formed Scales and Deposits: Types, Characteristics, and Relevant Industries. In: *Mineral Scales and Deposits: Scientific and Technological Approaches*. Elsevier Inc., pp. 3–23. DOI: 10.1016/B978-0-444-63228-9.00001-2.

[27] Hauksson, T., Thorhallsson, S., Gunnlaugsson, E., Albertsson, A. (1995). Control of Magnesium Silicate Scaling in District Heating Systems. In: *World Geothermal Congress*. Florence:, pp. 2487–2490.

[28] Li, C., Zhang, C., Zhang, W. (2019). The Inhibition Effect Mechanisms of Four Scale Inhibitors on the Formation and Crystal Growth of CaCO3 in Solution. *Scientific Reports*, 9(1), 13366. DOI: 10.1038/s41598-019-50012-7.

[29] el Nahrawy, A.M., Abou Hammad, A.B., Turky, G., Elnasharty, M.M.M., Youssef, A.M. (2015). Synthesis and Characterization of Hybrid Chitosan-Calcium Silicate Nanocomposite Prepared Using Sol-Gel Method. *International Journal of Advancement in Engineering, Technology and Computer Sciences*, 2(1), 9–14.

[30] Joni, I.M., Nulhakim, L., Vanitha, M., Panatarani, C. (2018). Characteristics of Crystalline Silica (SiO_2) Particles Prepared by Simple Solution Method Using Sodium Silicate (Na_2SiO_3) Precursor. *Journal of Physics: Conference Series*, 1080(1), 012006. DOI: 10.1088/1742-6596/1080/1/012006.

[31] Musić, S., Filipović-Vinceković, N., Sekovanić, L. (2011). Precipitation of Amorphous SiO_2 Particles and Their Properties. *Brazilian Journal of Chemical Engineering*, 28(01), 89–94. DOI: 10.1590/S0104-66322011000100011.

[32] Alexander, G.B., Heston, W.M., Iler, R.K. (1954). The Solubility of Amorphous Silica in Water. *The Journal of Physical Chemistry*, 58(6), 453–455. DOI: 10.1021/j150516a002.

[33] Osswald, J., Fehr, K.T. (2006). FTIR Spectroscopic Study on Liquid Silica Solutions and Nanoscale Particle Size Determination. *Journal of Materials Science*, 41(5), 1335–1339. DOI: 10.1007/s10853-006-7327-8.

[34] Oh, T., Choi, C.K. (2010). Comparison Between SiOC Thin Films Fabricated by Using Plasma Enhance Chemical Vapor Deposition and SiO2 Thin Films by Using Fourier Transform Infrared Spectroscopy. *Journal of the Korean Physical Society*, 56(4), 1150–1155. DOI: 10.3938/jkps.56.1150.

[35] Rashid, I., Daraghmeh, N.H., al Omari, M.M., Chowdhry, B.Z., Leharne, S.A., Hodali, H.A., Badwan, A.A. (2011). Magnesium Silicate. In: *Profiles of Drug Substances, Excipients and Related Methodology*. Academic Press Inc., pp. 241–285. DOI: 10.1016/B978-0-12-387667-6.00007-5.

[36] Jäger, C., Dorschner, J., Mutschke, H., Posch, T., Henning, T. (2003). Steps Toward Interstellar Silicate Mineralogy. VII. Spectral Properties and Crystallization Behaviour of Magnesium Silicates Produced by the Sol-Gel Method. *Astronomy and Astrophysics*, 408(1), 193–204. DOI: 10.1051/0004-6361:20030916.

[37] Hofmeister, A.M., Bowey, J.E. (2006). Quantitative Infrared Spectra of Hydrosilicates and Related Minerals. *Monthly Notices of the Royal Astronomical Society*, 367(2), 577–591. DOI: 10.1111/j.1365-2966.2006.09894.x.

[38] Jiang, W., Hua, X., Han, Q., Yang, X., Lu, L., Wang, X. (2009). Preparation of Lamellar Magnesium Hydroxide Nanoparticles via Precipitation Method. *Powder Technology*, 191(3), 227–230. DOI: 10.1016/j.powtec.2008.10.023.

[39] Choudhary, R., Koppala, S., Swamiappan, S. (2015). Bioactivity Studies of Calcium Magnesium Silicate Prepared From Eggshell Waste by Sol-gel Combustion Synthesis. *Journal of Asian Ceramic Societies*, 3(2), 173–177. DOI: 10.1016/j.jascer.2015.01.002.

[40] Galván-Ruiz, M., Hernández, J., Baños, L., Noriega-Montes, J., Rodríguez-García, M.E. (2009). Characterization of Calcium Carbonate, Calcium Oxide, and Calcium Hydroxide as Starting Point to the Improvement of Lime for Their Use in Construction. *Journal of Materials in Civil Engineering*, 21(11), 694–698. DOI: 10.1061/(ASCE)0899-1561(2009)21:11(694).

[41] Husain, S., Permitaria, A., Haryanti, N.H., Suryajaya, S. (2019). Synthesis and Characterization of Calcium Silicate From Rice Husk Ash and Snail Shell. *Jurnal Neutrino: Jurnal Fisika dan Aplikasinya*, 11(2), 45–51. DOI: 10.18860/neu.v11i2.6608.

[42] Sazali, R.A., Ramli, N.S., Sorbie, K.S., Boak, L.S. (2021). Impacts of Temperature on the Silicate Scale Morphologies Studies and Severity. *International Transaction Journal of Engineering, Management, & Applied Sciences & Technology*, 12(9), 1–16. DOI: 10.14456/ITJEMAST.2021.186.